

Observation of microscopic domain effects in the metal-insulator transition of thin-film NdNiO₃

Lucy S. Nathwani ,[†] Anne Ruperto,[†] Ashvini Vallipuram,[†] Abigail Y. Jiang,^{‡,†}
Grace A. Pan ,[†] Dan Ferenc Segedin ,[†] Ari B. Turkiewicz,[†] Charles M.
Brooks,[†] Jarad A. Mason ,^{*,¶} Qichen Song ,^{*,¶} and Julia A. Mundy ,^{*,†,‡}

[†]*Department of Physics, Harvard University, Cambridge, MA, 02138*

[‡]*John A. Paulson School of Engineering and Applied Sciences, Harvard University,
Cambridge, MA, 02138*

[¶]*Department of Chemistry and Chemical Biology, Harvard University, Cambridge, MA,
02138*

E-mail: mason@chemistry.harvard.edu; qichensong@g.harvard.edu; mundy@fas.harvard.edu

Abstract

Perovskite oxides can display correlated electrical, magnetic, and thermal properties; these properties can be further tuned in the thin film limit, making them leading contenders for next-generation electronics. Thin-film thermal measurements are challenging because techniques are dominated by the substrate. Here, frequency-domain thermoreflectance (FDTR) of an epitaxial NdNiO₃ thin film reveals a sharp change in out-of-plane thermal conductivity across the metal-to-insulator transition. Complementary frequency-domain photo-reflectance (FDPR) reveals a large change in ambipolar diffusivity of photoexcited carriers. Unlike the hysteresis seen in in-plane electrical resistance, out-of-plane thermal and charge transport show negligible hysteresis. We attribute this discrepancy to anisotropy in the percolative effects of nanoscale domains

across the transition as the film thickness approaches the domain length scale. We establish FDTR and FDPR as sensitive probes of quantum material phase transitions and demonstrate the potential of NdNiO₃ for thermal control and memory applications.

Keywords

hysteresis, microscopic domains, metal-insulator transitions, thermal transport, charge transport

Introduction

As the demand for miniaturized, energy-efficient electronics grows, materials that undergo temperature-driven metal-insulator transitions (MIT) have emerged as candidates for next-generation technologies, including thermal switches for heat regulation, smart windows for thermochromic glazing, nonvolatile memristors for data storage, and neuromorphic computing elements for brain-inspired computing.^{1–4} Among these, rare-earth perovskite nickelates, $R\text{NiO}_3$ ($R = \text{La, Pr, Nd...}$), are model systems due to their highly tunable phase transitions.^{5–8} In particular, neodymium nickelate, NdNiO₃, undergoes a first-order phase transition from a paramagnetic metallic state to an antiferromagnetic insulating state, with a concomitant change in the crystal structure at the highest temperature of the $R\text{NiO}_3$ series. It exhibits thermal hysteresis due to percolation across domains that emerge during the transition.^{9–11} In single crystal NdNiO₃, this transition occurs near 200 K. However, in the thin-film limit, the transition temperature can be tuned through epitaxial strain and film thickness,^{5,12–15} making it highly adaptable for integration into electronic devices. While most studies have focused on the electrical and magnetic properties of thin film NdNiO₃, its thermal properties are highly relevant for its practical applications in devices. Fully exploiting these materials in next-generation devices, however, requires an understanding of anisotropic charge and heat transport at the nanoscale, particularly as the thickness of the

film approaches the length scales of domain formation during the phase transition.

Measuring thermal transport in ultrathin films remains challenging due to the limited sensitivity of conventional bulk techniques, as traditional measurements of thermal conductivity using an applied heat source and a voltage measurement are dominated by substrate contributions.¹⁶ While 3ω techniques offer improved sensitivity to thin films, they require complex and invasive sample preparation, and lack spatial resolution.¹⁷ Non-contact optical reflectance-based techniques provide an alternative avenue that addresses these limitations.¹⁸ In particular, frequency-domain thermoreflectance (FDTR)^{19,20} is capable of measuring the thermal conductivity of films as thin as several tens of nanometers, while requiring only minimal sample preparation (i.e., depositing a metallic transducer). FDTR can even measure thermal transport in monolayer materials like graphene, depending on the film composition and the substrate.^{21,22} The same optical setup without a transducer layer can be used to perform frequency-domain photo-reflectance (FDPR), further allowing the charge and thermal transport to be probed simultaneously.²³

In this work, we use FDTR to measure the thermal conductivity of a 57.5 nm thick epitaxial NdNiO₃ film grown on a LaAlO₃ substrate across its metal-insulator transition, the thinnest such epitaxial oxide measured with FDTR to date. While we observe strong hysteresis in the in-plane electrical transport, consistent with prior measurements,^{9,12,24} we observe significantly reduced hysteresis in the thermal conductivity during heating and cooling cycles. We also perform the first demonstration of FDPR measurements on a thin film over a wide modulation-frequency bandwidth; we model the laser-induced charge transport as ambipolar diffusion, in which electrons and holes diffuse according to their density gradients before recombination. We observe a significant change in ambipolar diffusivity across the transition, accompanied by weaker hysteresis. The suppressed hysteresis in both thermal and charge transport is attributed to geometric anisotropy in the thin-film architecture, where the domain size is constrained by the film thickness, limiting percolation in the out-of-plane direction. These findings demonstrate the power of a local probe to resolve the nanoscale

phase separation that governs the dynamics of tunable MITs in thin-film correlated oxides.

Results and Discussion

In bulk single crystals of NdNiO_3 , the MIT is accompanied by a subtle structural transition from orthorhombic (Pbnm) to monoclinic ($\text{P}2_1/\text{n}$) symmetry (Fig. 1a);^{5,7,25} the transition has a thermal hysteresis of ~ 4 K. In epitaxial thin films, the hysteresis increases to ~ 30 K due to epitaxial strain.^{11,26} Electrical transport measurements of our thin-film sample show a sharp change from metallic to insulating behavior in bulk resistivity measurements upon cooling at $T_{\text{cool}} = 91$ K, and we observe the inverse change at $T_{\text{heat}} = 124$ K during heating (Fig. 1b). The biaxial compressive strain imposed by the LaAlO_3 substrate lowers T_{MIT} by over 70 K, consistent with prior observations of strain-induced suppression of T_{MIT} .^{5,12}

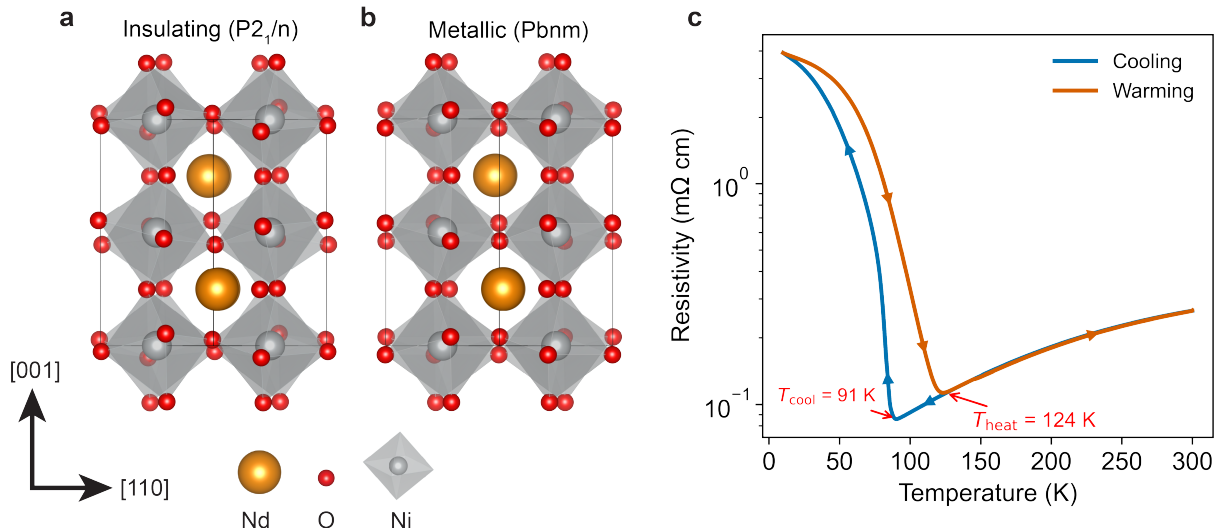


Figure 1: **a**, Distorted perovskite structure of NdNiO_3 in the insulating phase. **b**, The structure in the metallic phase. The changes in octahedral tilts drive the transition.⁷ **c**, Temperature-dependent resistance capturing the MIT (see Methods). T_{MIT} is 91 K during cooling and 124 K during heating. The film is 57.5 nm (150 unit cells) thick in the $(001)_{\text{PC}}$ direction, grown on LaAlO_3 (100) $_{\text{PC}}$.

We explore thermal and electronic transport through complementary techniques of FDTR and FDPR on the same sample. As illustrated in Fig. 2a, to isolate the thermal response of

the film, we perform FDTR measurements for a region coated with a gold transducer layer, which immediately converts electronic excitations into heat and ensures that the measured change in reflectance $\Delta R(\omega)$ is based only on the thermal properties of the sample (see Methods).^{19,20} To measure charge transport, we perform FDPR measurements on an adjacent uncoated region of the same sample; the photo-reflectance signal includes contributions from heat diffusion and charge transport. We then determine the ambipolar carrier diffusivity across the transition.

In FDTR, the thermoreflectance signal is proportional to the change in surface temperature of the gold transducer. The relative phase between the oscillations of the thermoreflectance signal and the pump modulation exhibits a distinct frequency dependence in the metallic phase compared to the insulating phase (Fig. 2b). According to the sensitivity analysis based on the Fourier heat conduction model, our FDTR measurement is exclusively sensitive to the out-of-plane thermal conductivity, κ_{\perp} (Fig. 2d). At high modulation frequencies, the phase shifts towards zero with increasing κ_{\perp} , while at low modulation frequencies, it shifts to more negative values with increasing κ_{\perp} (Fig. 2b). This relationship suggests that the out-of-plane thermal conductivity of the metallic phase is higher than that of the insulating phase, as expected.

In FDPR, the photo-reflectance from the bare sample is the sum of the carrier-induced and temperature-induced components, both of which are represented by complex numbers. As shown in Fig. 2c, at higher modulation frequencies, the carrier contribution can lower the overall phase lag compared to the temperature contribution alone, as carrier diffusion typically occurs much faster than heat diffusion. The different phase curves in the metallic and insulating states, especially at high modulation frequencies, are closely related to the difference in the carrier part of the signal. From the sensitivity analysis in Fig. 2e, we observe that the constant A_{ρ} that determines the magnitude of the carrier contribution to the signal, the carrier recombination time τ , and ambipolar diffusivity D_a are correlated, allowing us to fit only one of these three parameters reliably. Given that D_a is substantially more

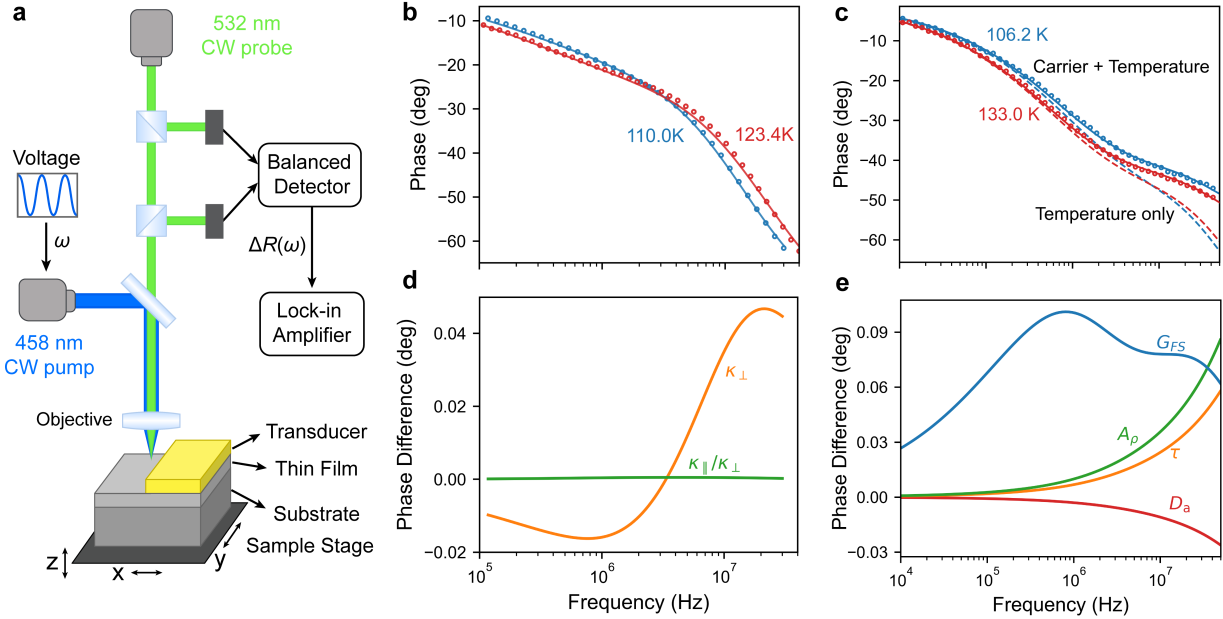


Figure 2: **a**, Schematic of an integrated frequency-domain thermoreflectance (FDTR) and frequency-domain photo-reflectance (FDPR) measurement setup. A continuous wave (CW) pump laser at 458 nm, power-modulated at a frequency $\omega/2\pi$, excites the sample. A CW probe laser at 532 nm reads out the perturbed reflectance. Both laser beams are focused to a 3 μm beam waist radius. The reference and reflected beams are first balanced and then detected by a balanced detector. The change in reflectance $\Delta R(\omega)$ is extracted from the output signal by a lock-in amplifier. FDTR and FDPR measurements are performed at the gold-coated (65.7 nm) and bare regions of the sample, respectively, with a piezoelectric stage being used to translate the sample in the xy-plane and to locate the beam focus along the z-axis. **b**, FDTR phase data (circles) in the metallic (123.4 K) and insulating (110.0 K) phases, along with best fits using the Fourier heat conduction model (lines). **c**, FDPR data in the metallic (133.0 K) and insulating (106.2 K) phases, along with best fits using the carrier and temperature model (solid lines); the phases of the temperature part of the signal are plotted in dashed lines. **d,e**, Sensitivity analysis for FDTR (**d**) and FDPR (**e**) data fitting at 110.0 K and 133.3 K, respectively. Specifically, κ_{\parallel} and κ_{\perp} correspond to the in-plane and out-of-plane thermal conductivity, respectively. G_{FS} is the thermal boundary conductance between the NdNiO₃ film and the LaAlO₃. A_{ρ} is related to the magnitude of the carrier contribution to the signal, τ is the carrier recombination time, and D_a is the ambipolar diffusivity. The phase difference is defined as the change in phase resulting from a +1% relative increase in the corresponding variable.

susceptible to changes in transport than both A_{ρ} and τ , we fix the values of A_{ρ} and τ and treat D_a along with the thermal boundary conduction between the thin film and substrate, G_{FS} , as fitting variables (see SI for details).

Analyzing both FDTR and FDPR data requires knowledge of substrate properties.

Therefore, we characterized the thermal properties of the LaAlO₃ substrate independently. We performed FDTR measurements on a LaAlO₃ substrate coated with a transducer layer (see Methods) and record its thermal conductivity and heat capacity over the temperature range of 80–140 K (Fig. 3a). The measured substrate heat capacity and thermal conductivity (Fig. 3a) agree well with literature values for the heat capacity and thermal conductivity of LaAlO₃.²⁷ Notably, our approach enables the simultaneous determination of both thermal conductivity and heat capacity from a single measurement. This is achieved by varying the modulation frequency over a wide range: at higher frequencies, the thermoreflectance's phase has a positive correlation with both thermal conductivity and heat capacity, while at lower frequencies, its dependence on thermal conductivity and heat capacity have opposite signs.

We then fix the substrate thermal conductivity and heat capacity in our heat conduction model and determine the out-of-plane thermal conductivity ($\kappa_{\perp,\text{tot}}$) of the NdNiO₃ thin film. We perform heating and cooling measurements between 80–140 K. Simultaneously fitting both κ and C_p for the film is challenging because of the high uncertainty and because these parameters are strongly correlated. Therefore, we fix the film's heat capacity using a Debye model derived from bulk heat capacity measurements on NdNiO₃ (see Fig. S16).^{24,28} With only the film's thermal conductivity as a free parameter, we achieve stable fits with uncertainty < 18%. Figure 3b shows the thermal conductivity κ of the thin film NdNiO₃ during cooling and heating cycles.

During cooling, the thermal conductivity $\kappa_{\perp,\text{tot}}$ of NdNiO₃ gradually decreases between 133.3 K and 123.3 K. Between 123.3 K and 110.0 K, it decreases more sharply by 33%, a phenomenon we describe as thermal switching. We compare the out-of-plane thermal conductivity to the predicted electronic contribution to the in-plane thermal conductivity using the Wiedemann–Franz law. It is important to recognize that Wiedemann–Franz law can fail in correlated oxides,^{29,30} where non-Fermi-liquid transport might emerge.³¹ Consequently, we regard the predicted electronic thermal conductivity as a comparative indicator of in-plane heat transport. We calculate $\kappa_{\parallel,\text{el}} = L\sigma T$, where L is the Lorenz number, σ is the separately

measured in-plane electrical conductivity (Fig. 1a) and T is the temperature. In principle, we expect no anisotropy in the properties of bulk NdNiO₃, so we attribute the differences in thermal conductivity to finite scaling in the thin film limit.

On cooling, we observe the onset of thermal switching in $\kappa_{\perp,\text{tot}}$ more than 20 K higher in temperature than in $\kappa_{||,\text{el}}$. The heating curve of $\kappa_{\perp,\text{tot}}$ closely matches the cooling curve across the transition, suggesting that this transition temperature anisotropy arises from weak hysteresis in the out-of-plane direction. Consistent with this behavior, the out-of-plane ambipolar mobility during heating and cooling from FDPR decreases sharply from 120 K to 110 K and changes by much smaller amounts for $T < 110$ K (Fig. 3c), which reinforces the idea that an electronic phase transition occurs at T_{switch} . The DC contribution of the reflectance from the bare sample, related to the dielectric constants of the thin film, also shows a sharp discontinuity at around 115 K, providing additional evidence for the electronic phase transition occurring near T_{switch} (Fig. S12). Together, these measurements show that the transition temperature and the associated hysteresis measured in the out-of-plane direction differ substantially from those observed in the in-plane direction.

Both epitaxial strain and film thickness can tune the MIT in NdNiO₃, so we first consider whether differing strain in the out-of-plane direction can lead to anisotropic hysteresis. We expect that the film is under compressive strain in the in-plane direction due to the substrate, and therefore it is under tensile strain in the out-of-plane direction.³² While bulk NdNiO₃ has a hysteresis loop width of ~ 4 K,²⁶ both compressive and tensile strain on thin films increase the hysteresis loop width to > 10 K.³³ We therefore expect hysteresis in the in-plane and out-of-plane directions, and anisotropic strain effects should not eliminate hysteresis in the out-of-plane direction. To understand the origin of the discrepancy, we then consider the length scale of the FDTR and FDPR measurements compared to electrical resistivity measurements, understanding the dimensionality of the transition in the thin-film limit. In NdNiO₃, nanoscale insulating domains begin to nucleate tens of Kelvin above the macroscopic transition, with domain sizes on the order of 100–300 nm.^{9,34} Electrical resistivity

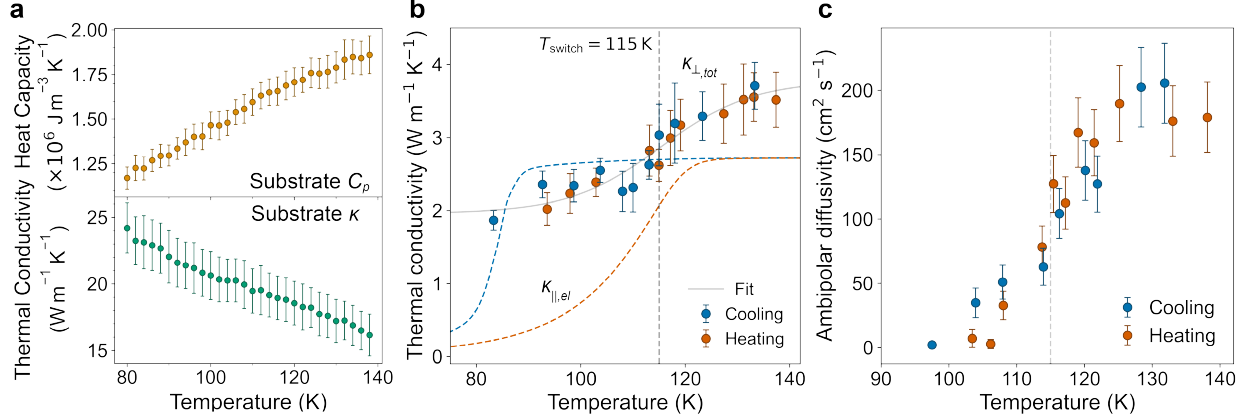


Figure 3: **a**, The thermal conductivity and heat capacity of the substrate LaAlO_3 measured using FDTR. **b**, Out-of-plane thermal conductivity, $\kappa_{\perp,\text{tot}}$, of thin film NdNiO_3 as a function of temperature, measured using FDTR over three cooling and two heating cycles (see Fig. S6 for the full data). The electronic contribution to in-plane thermal conductivity, $\kappa_{||,\text{el}}$, predicted using the Wiedemann–Franz law is plotted as dashed lines. The hysteresis is weaker in the out-of-plane direction than in the in-plane direction, highlighting the anisotropy of the thin-film geometry. A modified logistic function, $f(T) = a [1 + e^{-b(T - T_{\text{switch}})}]^{-1} + c$, is used to fit the thermal conductivity trend (gray line). The thermal switching temperature T_{switch} is found to be 115 K. **c**, The ambipolar diffusivity of NdNiO_3 , measured using FDPR, across the metal-insulator transitions during cooling and heating. The dashed line corresponds to $T_{\text{switch}} = 115 \pm 4 \text{ K}$, with the standard deviation obtained from a bootstrap analysis. Fixed parameters $A_\rho = 8 \times 10^{-25} \text{ m}^3 \text{K}$ and $\tau = 0.11 \text{ ns}$ are chosen to minimize fitting residuals across all temperatures.

measurements average over several millimeters in the in-plane direction, measuring transport crossing hundreds of domains (Fig. 4b). Across the transition, percolation pathways must form before significant changes in conductivity are observed, delaying the onset of the transition and causing hysteresis.^{11,25}

In contrast, our optical reflectance-based measurements probe out-of-plane transport in films where the average domain size exceeds the film thickness (57.5 nm). Although the laser beam, which has a 3 μm radius, covers many domains laterally, it measures transport through single phases, averaged over those domains. This columnar domain geometry reduces sensitivity to percolation and interface effects, resulting in the observed reduced hysteresis (Fig. 4c). This phenomenon is further corroborated by replicated measurement on a 20.6-nm-thick NdNiO_3 film on LaAlO_3 (Fig. S10), which demonstrates a similar lack of hys-

teresis in the out-of-plane thermal conductivity. FDTR and FDPR in a thin film geometry are therefore uniquely sensitive to domain emergence in a phase transition, capturing the early onset of localized phase separation that precedes changes in the macroscopic properties. Although the diffraction limit prevents us from directly resolving the thermal conductivity of a single domain or right at the interface, our approach uniquely provides access to the cross-plane thermal conductivity, which—when combined with the mapped domain structures reported in previous studies^{10,25,34,35}—allows us to understand how domains govern transport properties.

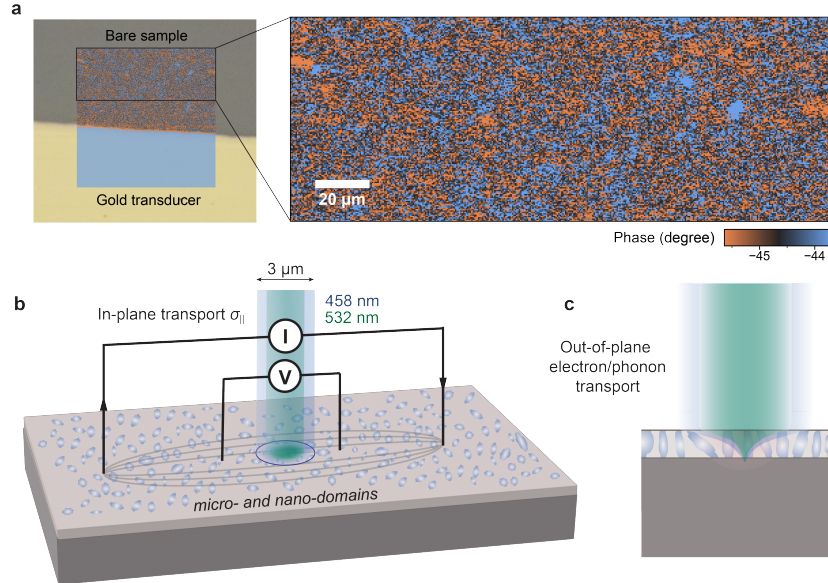


Figure 4: **a**, FDPR mapping of the sample during cooling over an area of $200 \mu\text{m} \times 200 \mu\text{m}$ at 113 K with a modulation frequency of 14.4 MHz, overlaid with the microscope image. The sharp phase contrast corresponds to the boundary of the gold transducer. The region in the black box on the bare sample is magnified on the right. The color represents the FDPR phase. The beam is too large to directly observe domains, which we expect to be 100-300 nm, but we can observe lateral fluctuations in the signal to high resolution. **b**, Qualitative (not to scale) schematic representing the formation of insulating domains in NdNiO₃ near the phase transition temperature. FDPR probes out-of-plane electron transport on a length scale covering several domains, whereas the electrical resistance measurement aggregates in-plane contributions from electrons percolating across on the order of 10^3 domains. **c**, Cross-sectional view of the beam penetration and domain formation (not to scale). Domains form instantaneously across the film thickness, directly creating single-phase transport channels without metal-insulator interfaces; hence, out-of-plane thermal and electron transport exhibits low hysteresis.

Our study reveals a microscopic, domain-mediated phase transition in NdNiO₃ preceding the MIT transition observed via bulk transport measurement. Thermal switching occurs at a temperature significantly above the metal-insulator transition identified by in-plane electrical transport measurement, with significantly reduced hysteresis. The thin film geometry plays a significant role in the reduced hysteresis, as the length scale of the domains formed during the transition is larger than the film thickness, allowing us to reduce percolation across domains in the out-of-plane direction. While much research on NdNiO₃ has been dedicated to tuning the hysteresis and transition temperature of the MIT, the anisotropy of the thin-film geometry has yet to be addressed and presents another way to tune the properties of the MIT. These results position NdNiO₃ thin films within a growing class of correlated oxides that exhibit nontrivial transport behavior across electronic phase transitions. Violations of the Wiedemann–Franz law observed in VO₂ nanowires near the MIT³⁰ suggest the involvement of unconventional quasiparticles or other strongly correlated transport phenomena.³⁶ The unusual behavior of the reduced dimensionality in VO₂ nanowires highlights the macroscopic effects of fundamental length scales in correlated oxides with phase transitions. Our findings open new avenues for exploring the role of geometrical confinement and domain structure in such materials, advancing NdNiO₃ thin films as compelling candidates for realizing passive thermal switches and non-volatile memristors.

Our work demonstrates that FDTR and FDPR offer unique capabilities for probing phase transitions in thin films where the domain sizes exceed the film thickness. In contrast to bulk resistivity, which probes in-plane transport percolating across many domains, our reflectance-based measurements are more sensitive to the local emergence and distribution of metallic and insulating domains. FDTR measurements in ultrathin films, therefore, primarily average transport across single domains, minimizing percolative effects and hysteresis. The sharp features observed in both thermal transport and ambipolar diffusivity (D_a) near T_{switch} with weak hysteresis confirm the differences in the measurement due to the geometry of FDTR and FDPR. Spatial FDPR mapping further reveals nanoscale phase coexistence

near the transition, reinforcing a picture of spatially inhomogeneous, domain-driven phase evolution.^{9,11,25,34} These insights demonstrate that FDTR is a powerful probe of phase transitions in complex oxides, enabling access to out-of-plane transport properties in regimes inaccessible to traditional bulk methods.

Beyond this central result, we introduce several methodological advances. We demonstrate that FDTR can simultaneously measure the thermal conductivity and heat capacity of a bulk substrate material (in this case, LaAlO₃) across a wide temperature range. We also report the first use of FDPR to extract ambipolar carrier diffusivity in a thin film system. The observed drop in D_a across the same temperature range as the thermal transition confirms the co-evolution of electronic and thermal transport across the MIT. This combined FDTR/FDPR framework opens avenues for studying nanoscale phase transitions, domain dynamics, and anisotropic transport in complex oxides, both in equilibrium and under external stimuli such as strain or electric fields.

Methods

Sample Preparation

Thin-film NdNiO₃ was synthesized on LaAlO₃ (100) using ozone-assisted molecular-beam epitaxy (MBE).³⁷ LaAlO₃ has a smaller lattice mismatch than other possible substrates, enabling the thickest film without relaxation. During the deposition, the substrate temperature was kept at 555°C and the chamber pressure was maintained at $\sim 1.3 \times 10^{-6}$ torr distilled ozone (Heeg Vacuum Engineering). We expect biaxial compressive strain of 0.4%. The unit cell volume change across the transition is negligible. *In-situ* reflection high-energy electron diffraction (RHEED), X-ray diffraction, and X-ray reflectivity measurements (PANalytical Empyrean X-Ray Diffractometer) demonstrate a highly crystalline, epitaxially strained sample with a smooth surface, with measured thickness 57.5 nm, approximately 150 unit cells (see Fig. S1,S2). We measured the sample resistance (Fig. 1) via a standard 4-probe AC

resistance measurement in a physical property measurement system (PPMS).

To determine the thermal properties of the substrate, we coated a sample of LaAlO₃ (Shinkosha) with a transducer layer. We deposited 56 nm Au with a 2.6 nm Cr adhesion layer and confirmed the thickness using x-ray reflectivity (PANalytical Empyrean X-Ray Diffractometer). We found that the Cr adhesion layer in the LaAlO₃ sample created nonequilibrium electron-phonon coupling in the transducer layer and increased the phase lag for modulation frequencies above 10 MHz;³⁸ this effect is beyond the scope of our model. We still obtained accurate thermal parameters from lower modulation frequencies in the LaAlO₃ sample, as the measurement of the substrate properties was sensitive to the phase at lower modulation frequencies (see Fig. S13).

We performed FDTR and FDPR measurements on the same sample of NdNiO₃ by coating half of the sample with a transducer layer. We deposited a transducer layer over a small region of the sample's surface, leaving much of the sample uncovered (see Fig. 2). For the NdNiO₃ sample, we deposited 65.7 nm Au with a 1.8 nm Ti adhesion layer using electron-beam evaporation (Denton E-beam Evaporator). We confirmed the thickness with X-ray reflectivity as above. Based on the results from the substrate FDTR, we chose to use a Ti adhesion layer for the NdNiO₃ to eliminate transducer electron-phonon coupling. We could then model the phase at higher modulation frequencies where it is sensitive to the film's properties, as shown in Fig. 2c. The transducer we deposited on the NdNiO₃ film had a roughness of 14.16 Å (Fig. S3). These transducer layers were straightforward to model for our desired modulation frequencies, as gold is frequently used for FDTR, and its thin film thermal conductivity and heat capacity are known.³⁹ The gold coating thermal conductivity was independently measured using the 4-point probe method.

FDTR and FDPR

We use the FDTR and FDPR setup supplied by Fourier Scientific. To change the pump frequency, we modulate the voltage of a 458 nm 20 mW pump laser (Coherent OBIS LX

fiber laser) and sweep the modulation frequency. The incident pump power is measured to be 17.3 mW. We also tested lower pump powers and observed similar thermal conductivity values. We record the amplitude and phase of $\Delta R(\omega)$ using a 532 nm 15 mW continuous-wave probe laser (Coherent OBIS LS laser) and a lock-in amplifier (Zurich Instruments HF2LI).

Both the pump and probe beams are nearly isotropic with Gaussian spatial profiles; the $1/e^2$ radius of the probe beam is 2.98 μm . To minimize the noise in the probe signal, we rotate a half-wave plate in the probe beam path before it reaches the sample, which minimizes the difference in the intensity of the reference and reflected probe beams. Before we make a measurement, we measure the phase of the pump beam to subtract it from the measured phase. When measuring, we send the probe beams before and after reflection from the sample to a balanced photodetector. After sending the signal from the balanced detector to the lock-in amplifier,¹⁹ we obtain $\Delta R(\omega)$ for a range of frequencies ω . We controlled the temperature using a flow cryostat (Instec HCP421V).

For substrate measurements using FDTR, we choose C_p and κ_z as the fitting variables in the fitting analysis. For thin-film measurements, we choose κ_{\perp} as the fitting variable for FDTR, and D_a and G_{FS} for FDPR. Specifically, we used the temperature-dependent κ_{\perp} obtained from FDTR as an input parameter used in the FDPR modeling. To extract the fitting variables of interest, we fit the phase of $\Delta R(\omega)$ using a nonlinear least-squares optimization to minimize the difference between the measured phase of $\Delta R(\omega)$ and the model prediction. Further details of the FDPR modeling formalism, along with additional parameters used in both FDTR and FDPR modeling, can be found in the SI.

Acknowledgement

The authors thank Aaron J. Schmidt for helpful discussions. L.S.N. thanks Suzanne Smith and Jennifer Hoffman for their feedback on the manuscript. This project was primarily supported by the US Department of Energy, Office of Basic Energy Sciences, Division of

Materials Sciences and Engineering, under Award No. DE-SC0021925. We also acknowledge support from the National Science Foundation with award DMR-2323970. This work was performed in part at the Harvard University Center for Nanoscale Systems (CNS); a member of the National Nanotechnology Coordinated Infrastructure Network (NNCI), which is supported by the National Science Foundation under NSF award no. ECCS-2025158. Q.S., L.S.N., and A.R. acknowledge support from the Harvard Quantum Initiative. A.Y.J., G.A.P., and D.F.S. acknowledge support from the NSF Graduate Research Fellowship Grant DGE-1745303. A.Y.J. and G.A.P. were also supported by the Paul & Daisy Soros Fellowship for New Americans, and A.Y.J. by the Ford Foundation. J.A.M. acknowledges funding from the Star Friedman Fund at Harvard University. L.S.N. and A.R. acknowledge support from the Herchel Smith Undergraduate Science Research Program. Generative A.I. was used in the codes to create plots for the figures.

Supporting Information Available

X-ray diffraction and X-ray reflectivity of NdNiO₃; X-ray reflectivity of the transducer layer; AFM of NdNiO₃; full derivation of the carrier and temperature model for FDPR signals, and data analysis.

References

- (1) Wen, C.; Feng, L.; Li, Z.; Bai, J.; Wang, S.; Gao, X.; Wang, J.; Yao, W. A review of the preparation, properties and applications of VO₂ thin films with the reversible phase transition. *Frontiers in Materials* **2024**, *11*, 1341518.
- (2) Haddad, E.; Kruzelecky, R. V.; Murzionak, P.; Jamroz, W.; Tagziria, K.; Chaker, M.; Ledrogoff, B. Review of the VO₂ smart material applications with emphasis on its use for spacecraft thermal control. *Frontiers in Materials* **2022**, *9*, 1013848.

- (3) Xia, Q.; Yang, J. J. Memristive crossbar arrays for brain-inspired computing. *Nature Materials* **2019**, *18*, 309–323.
- (4) Imada, M.; Fujimori, A.; Tokura, Y. Metal-insulator transitions. *Reviews of Modern Physics* **1998**, *70*, 1039–1263.
- (5) Catalano, S.; Gibert, M.; Fowlie, J.; Íñiguez, J.; Triscone, J.-M.; Kreisel, J. Rare-earth nickelates RNiO_3 : thin films and heterostructures. *Reports on Progress in Physics* **2018**, *81*, 046501, Publisher: IOP Publishing.
- (6) Alonso, J. A.; Martínez-Lope, M. J.; Casais, M. T.; García-Muñoz, J. L.; Fernández-Díaz, M. T. Room-temperature monoclinic distortion due to charge disproportionation in R NiO_3 perovskites with small rare-earth cations ($\text{R} = \text{Ho}$, Y , Er , Tm , Yb , and Lu): A neutron diffraction study. *Physical Review B* **2000**, *61*, 1756–1763.
- (7) García-Muñoz, J. L.; Aranda, M. A. G.; Alonso, J. A.; Martínez-Lope, M. J. Structure and charge order in the antiferromagnetic band-insulating phase of NdNiO_3 . *Physical Review B* **2009**, *79*, 134432.
- (8) Liu, J.; Kargarian, M.; Kareev, M.; Gray, B.; Ryan, P. J.; Cruz, A.; Tahir, N.; Chuang, Y.-D.; Guo, J.; Rondinelli, J. M.; Freeland, J. W.; Fiete, G. A.; Chakhalian, J. Heterointerface engineered electronic and magnetic phases of NdNiO_3 thin films. *Nature Communications* **2013**, *4*, 2714.
- (9) Preziosi, D.; Lopez-Mir, L.; Li, X.; Cornelissen, T.; Lee, J. H.; Trier, F.; Bouzehouane, K.; Valencia, S.; Gloter, A.; Barthélémy, A.; Bibes, M. Direct mapping of phase separation across the metal–insulator transition of NdNiO_3 . *Nano Letters* **2018**, *18*, 2226–2232.
- (10) Mattoni, G.; Zubko, P.; Maccherozzi, F.; van der Torren, A.; Boltje, D. B.; Hadjimichael, M.; Manca, N.; Catalano, S.; Gibert, M.; Liu, Y.; Aarts, J.; Triscone, J.-M.;

- Dhesi, S. S.; Caviglia, A. D. Striped nanoscale phase separation at the metal–insulator transition of heteroepitaxial nickelates. *Nature Communications* **2016**, *7*, 13141.
- (11) Lee, J. H.; Trier, F.; Cornelissen, T.; Preziosi, D.; Bouzehouane, K.; Fusil, S.; Valencia, S.; Bibes, M. Imaging and Harnessing Percolation at the Metal–Insulator Transition of NdNiO₃ Nanogaps. *Nano Letters* **2019**, *19*, 7801–7805, Publisher: American Chemical Society.
- (12) Zhang, J. Y.; Kim, H.; Mikheev, E.; Hauser, A. J.; Stemmer, S. Key role of lattice symmetry in the metal-insulator transition of NdNiO₃ films. *Scientific Reports* **2016**, *6*, 23652.
- (13) Laffez, P.; Lebedev, O. I.; Ruello, P.; Desfeux, R.; Banerjee, G.; Capon, F. Evidence of strain induced structural change in hetero-epitaxial NdNiO₃ thin films with metal-insulator transition. *The European Physical Journal Applied Physics* **2004**, *25*, 25–31.
- (14) Wang, L.; Dash, S.; Chang, L.; You, L.; Feng, Y.; He, X.; Jin, K.-j.; Zhou, Y.; Ong, H. G.; Ren, P.; Wang, S.; Chen, L.; Wang, J. Oxygen Vacancy Induced Room-Temperature Metal–Insulator Transition in Nickelate Films and Its Potential Application in Photovoltaics. *ACS Applied Materials & Interfaces* **2016**, *8*, 9769–9776, PMID: 27025257.
- (15) Shi, Y.; Chen, L.-Q. Thermodynamics of strain engineering in RNiO₃ (R = Sm , Nd). *Physical Review B* **2024**, *110*, 205117.
- (16) Grissonnanche, G.; Pan, G. A.; LaBollita, H.; Segedin, D. F.; Song, Q.; Paik, H.; Brooks, C. M.; Beauchesne-Blanchet, E.; Santana González, J. L.; Botana, A. S.; Mundy, J. A.; Ramshaw, B. J. Electronic band structure of a superconducting nickelate probed by the Seebeck coefficient in the disordered limit. *Physical Review X* **2024**, *14*, 041021.

- (17) Cahill, D. G. Thermal conductivity measurement from 30 to 750 K: the 3ω method. *Review of Scientific Instruments* **1990**, *61*, 802–808.
- (18) Oh, D.-W.; Ko, C.; Ramanathan, S.; Cahill, D. G. Thermal conductivity and dynamic heat capacity across the metal-insulator transition in thin film VO_2 . *Applied Physics Letters* **2010**, *96*, 151906.
- (19) Yang, J.; Maraglino, C.; Schmidt, A. J. Thermal property microscopy with frequency domain thermoreflectance. *Review of Scientific Instruments* **2013**, *84*, 104904.
- (20) Schmidt, A. J.; Cheaito, R.; Chiesa, M. A frequency-domain thermoreflectance method for the characterization of thermal properties. *Review of Scientific Instruments* **2009**, *80*, 094901.
- (21) Yang, J.; Ziade, E.; Schmidt, A. Imaging Thermal Transport in Graphene. *Journal of Heat Transfer* **2015**, *137*, 020901.
- (22) Akura, Y.; Ikeda, Y.; Matsunaga, Y.; Shimofuri, M.; Banerjee, A.; Tsuchiya, T.; Hiratani, J. Frequency-domain thermoreflectance with beam offset without the spot distortion for accurate thermal conductivity measurement of anisotropic materials. *Review of Scientific Instruments* **2025**, *96*, 014902.
- (23) Song, Q.; Warkander, S.; Huberman, S. C. Probing carrier and phonon transport in semiconductors all at once through frequency-domain photoreflectance. *Physical Review Applied* **2024**, *21*, 034044.
- (24) Hooda, M.; Yadav, C. Electronic properties and the nature of metal–insulator transition in NdNiO_3 prepared at ambient oxygen pressure. *Physica B: Condensed Matter* **2016**, *491*, 31–36.
- (25) Gomes, M. M.; Manjunath, B.; Vilarinho, R.; Bassou, A. A.; Silva, B.; Oliveira, J.; Çaha, I.; Deepak, F. L.; Almeida, B.; Almeida, A.; Kreisel, J.; Tavares, P. B.; Íñiguez, J.;

- Moreira, J. A. Structural percolation evolution throughout the metal-to-insulator transition in NdNiO₃. *Phys. Rev. B* **2024**, *109*, 224109.
- (26) Catalan, G.; Bowman, R. M.; Gregg, J. M. Metal-insulator transitions in NdNiO₃ thin films. *Physical Review B* **2000**, *62*, 7892–7900.
- (27) Schnelle, W.; Fischer, R.; Gmelin, E. Specific heat capacity and thermal conductivity of NdGaO₃ and LaAlO₃ single crystals at low temperatures. *Journal of Physics D: Applied Physics* **2001**, *34*, 846–851.
- (28) Barbata, V. B.; Jardim, R. F.; Torikachvili, M. S.; Escote, M. T.; Cordero, F.; Pontes, F. M.; Trequattrini, F. Metal-insulator transition in Nd_{1-x}Eu_xNiO₃ probed by specific heat and anelastic measurements. *Journal of Applied Physics* **2011**, *109*, 07E115.
- (29) Ronning, F.; Hill, R. W.; Sutherland, M.; Hawthorn, D. G.; Tanatar, M. A.; Paglione, J.; Taillefer, L.; Graf, M. J.; Perry, R. S.; Maeno, Y.; Mackenzie, A. P. Thermal Conductivity in the Vicinity of the Quantum Critical End Point in Sr₃Ru₂O₇. *Phys. Rev. Lett.* **2006**, *97*, 067005.
- (30) Lee, S.; Hippalgaonkar, K.; Yang, F.; Hong, J.; Ko, C.; Suh, J.; Liu, K.; Wang, K.; Urban, J. J.; Zhang, X.; Dames, C.; Hartnoll, S. A.; Delaire, O.; Wu, J. Anomalously low electronic thermal conductivity in metallic vanadium dioxide. *Science* **2017**, *355*, 371–374.
- (31) Mahajan, R.; Barkeshli, M.; Hartnoll, S. A. Non-Fermi liquids and the Wiedemann-Franz law. *Phys. Rev. B* **2013**, *88*, 125107.
- (32) Wang, L.; Ju, S.; You, L.; Qi, Y.; Guo, Y.-w.; Ren, P.; Zhou, Y.; Wang, J. Competition between strain and dimensionality effects on the electronic phase transitions in NdNiO₃ films. *Scientific Reports* **2015**, *5*, 18707.

- (33) Scherwitzl, R.; Zubko, P.; Lezama, I. G.; Ono, S.; Morpurgo, A. F.; Catalan, G.; Triscone, J. Electric-Field Control of the Metal-Insulator Transition in Ultrathin NdNiO₃ Films. *Advanced Materials* **2010**, *22*, 5517–5520.
- (34) Bisht, R. S.; Samanta, S.; Raychaudhuri, A. K. Phase coexistence near the metal–insulator transition in a compressively strained NdNiO₃ film grown on LaAlO₃: Scanning tunneling, noise, and impedance spectroscopy studies. *Physical Review B* **2017**, *95*, 115147.
- (35) Li, J.; Pelliciari, J.; Mazzoli, C.; Catalano, S.; Simmons, F.; Sadowski, J. T.; Levitan, A.; Gibert, M.; Carlson, E.; Triscone, J.-M.; Wilkins, S.; Comin, R. Scale-invariant magnetic textures in the strongly correlated oxide NdNiO₃. *Nature Communications* **2019**, *10*, 4568, Publisher: Nature Publishing Group.
- (36) Zhang, J.; Levenson-Falk, E. M.; Ramshaw, B. J.; Bonn, D. A.; Liang, R.; Hardy, W. N.; Hartnoll, S. A.; Kapitulnik, A. Anomalous thermal diffusivity in underdoped YBa₂Cu₃O_{6+x}. *Proceedings of the National Academy of Sciences* **2017**, *114*, 5378–5383.
- (37) Pan, G. A. et al. Synthesis and electronic properties of Nd_{n+1}Ni_nO_{3n+1} Ruddlesden-Popper nickelate thin films. *Physical Review Materials* **2022**, *6*, 055003.
- (38) Wilson, R. B.; Cahill, D. G. Anisotropic failure of Fourier theory in time-domain thermoreflectance experiments. *Nature Communications* **2014**, *5*, 5075.
- (39) Yang, J.; Ziade, E.; Schmidt, A. J. Modeling optical absorption for thermoreflectance measurements. *Journal of Applied Physics* **2016**, *119*, 095107.
- (40) Yang, J.; Ziade, E.; Schmidt, A. J. Uncertainty analysis of thermoreflectance measurements. *Review of Scientific Instruments* **2016**, *87*, 014901.
- (41) Katsufuji, T.; Okimoto, Y.; Arima, T.; Tokura, Y.; Torrance, J. B. Optical spectroscopy of the metal-insulator transition in NdNiO₃. *Physical Review B* **1995**, *51*, 4830–4835.

- (42) Ruppen, J.; Teyssier, J.; Peil, O. E.; Catalano, S.; Gibert, M.; Mravlje, J.; Triscone, J.-M.; Georges, A.; Van Der Marel, D. Optical spectroscopy and the nature of the insulating state of rare-earth nickelates. *Physical Review B* **2015**, *92*, 155145.
- (43) Stewart, M. K. Mott Physics near the Insulator-To-Metal Transition in NdNiO₃. *Physical Review Letters* **2011**, *107*, 176401.
- (44) Qazilbash, M. M.; Brehm, M.; Chae, B.-G.; Ho, P.-C.; Andreev, G. O.; Kim, B.-J.; Yun, S. J.; Balatsky, A. V.; Maple, M. B.; Keilmann, F.; Kim, H.-T.; Basov, D. N. Mott transition in VO₂ revealed by infrared spectroscopy and nano-imaging. *Science* **2007**, *318*, 1750–1753.
- (45) <https://github.com/qichensong/sco-thermal>.
- (46) Wilson, R. B.; Feser, J. P.; Hohensee, G. T.; Cahill, D. G. Two-channel model for nonequilibrium thermal transport in pump-probe experiments. *Phys. Rev. B* **2013**, *88*, 144305.

Supplemental Materials

Characterization of NdNiO₃ Film

Film Measurements

We measured the thickness and roughness of the film *in situ* and after the film growth. We used reflection high-energy electron diffraction (RHEED) to characterize the film *in situ*. Figure S1 shows the diffraction pattern of the film during growth in the (100) and (110) orientations. The pattern reveals a smooth, epitaxial film. Figure S2a shows the film's X-ray diffraction pattern, taken after growth. The peaks are consistent with epitaxial NdNiO₃ in the (001) orientation. The best fit for the X-ray reflectivity curve (Fig. S2b) shows the film to be 57.5 nm thick with a roughness of 6.5 Å. We examine the surface with atomic force microscopy (AFM), Fig. S3a. Terracing from the substrate miscut and some defects in the surface are visible. We measured bulk electrical transport (Fig. 1) on a Quantum Design Physical Property Measurements System (PPMS) by applying 0.01 mA AC at 18.31 Hz via wire-bonded contacts .

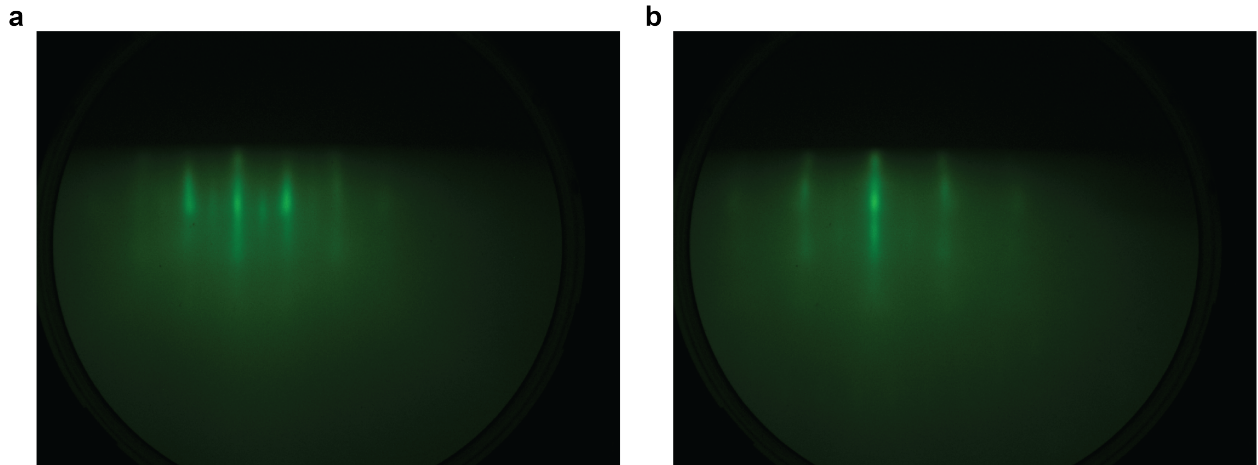


Figure S1: Reflection high-energy electron diffraction (RHEED) of NdNiO₃ on LaAlO₃ during MBE growth. Patterns recorded in the **a**, (110) orientation and **b**, (100) orientation.

Coating Measurements

The X-ray reflectivity (Fig. S2c) and AFM (Fig. S2b) of the gold-coated surface are also shown. The best fit for the X-ray reflectivity showed the coating to be 65.7 nm of gold and 1.8 nm of titanium, with a surface roughness of 14.16 Å (Fig. S2,S3). AFM confirms that the terracing is still visible, but the surface is slightly rougher overall, and there are still defects.

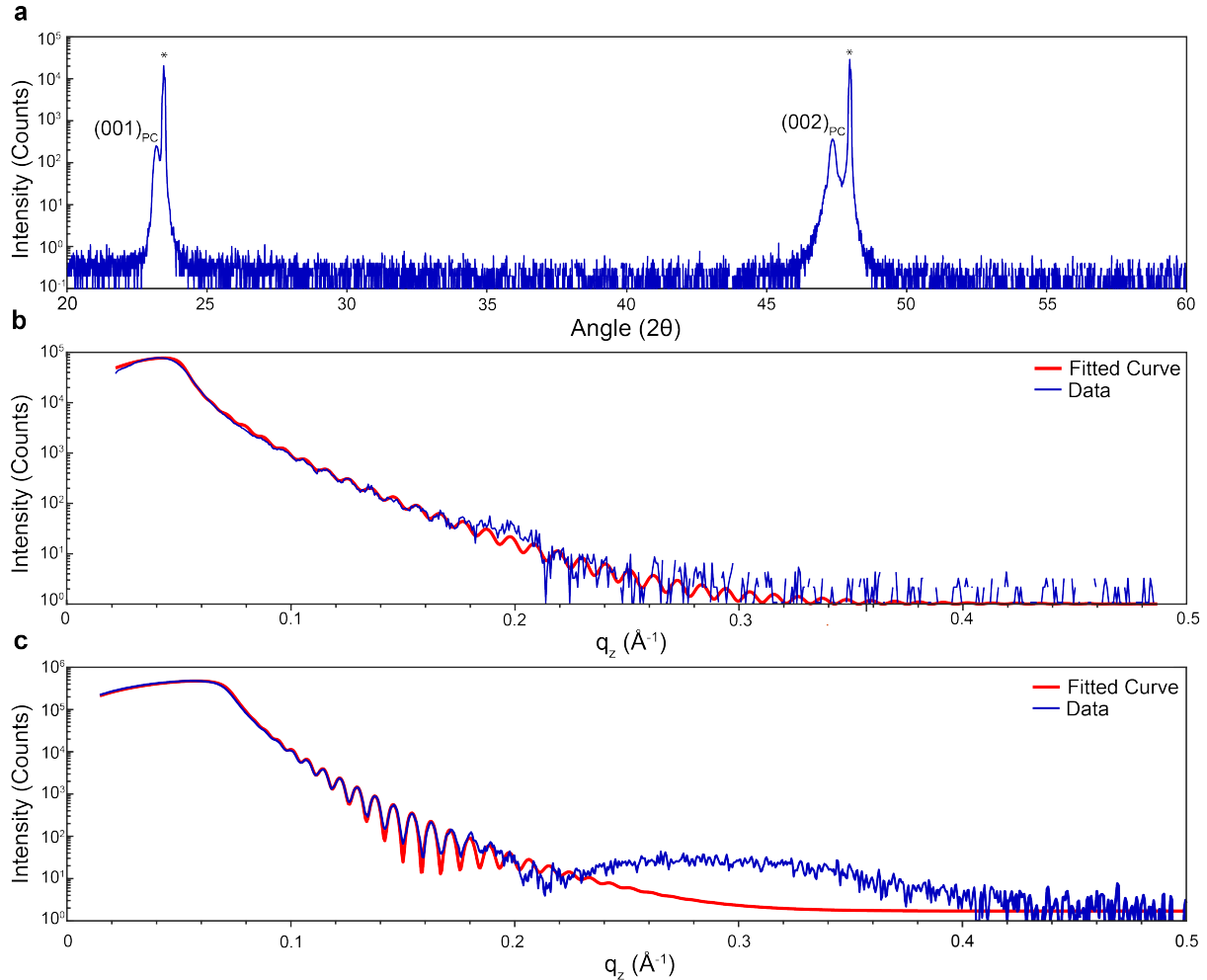


Figure S2: **a**, X-ray diffraction showing epitaxial NdNiO₃ $(001)_{PC}$ peaks. The asterisks denote LaAlO₃ (100) substrate peaks. **b**, X-ray reflectivity of the film after growth with the best fit overlaid. **c**, The X-ray reflectivity of the Au/Ti coating with the best fit curve overlaid. The bump after the oscillations is due to the silicon sample holder.

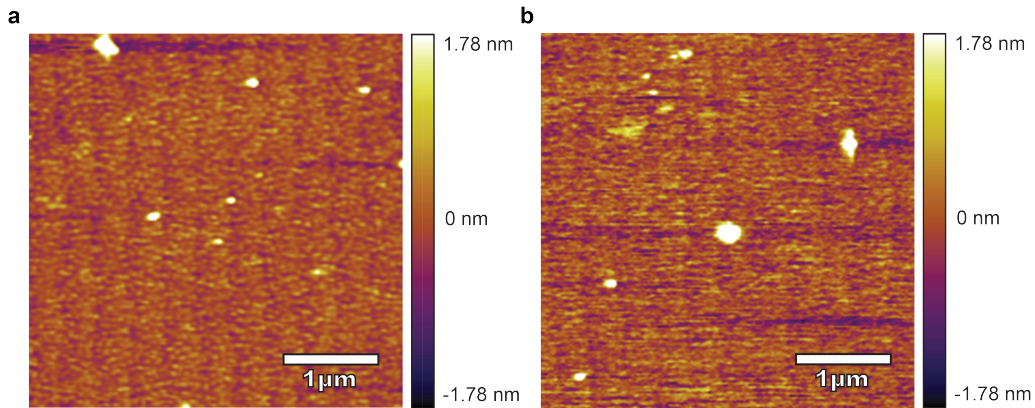


Figure S3: **a**, AFM characterization of NdNiO₃ film showing defects (bright spots) along with terracing due to the substrate miscut (vertical striping). **b**, AFM characterization of the NdNiO₃ film after being coated. The film is slightly rougher overall, but the terracing is still visible, and there are still surface defects.

Mapping FDPR Phase Fluctuations at Room Temperature

To attribute the regions we observe in Fig. 4 to phase separation, we recorded a FDPR phase map using a smaller beam size on the same sample at room temperature to measure the length scale of its fluctuations. We observe featureless, noise-induced fluctuations on a much smaller length scale, confirming that the domains we observe at the transition temperature are related to the MIT.

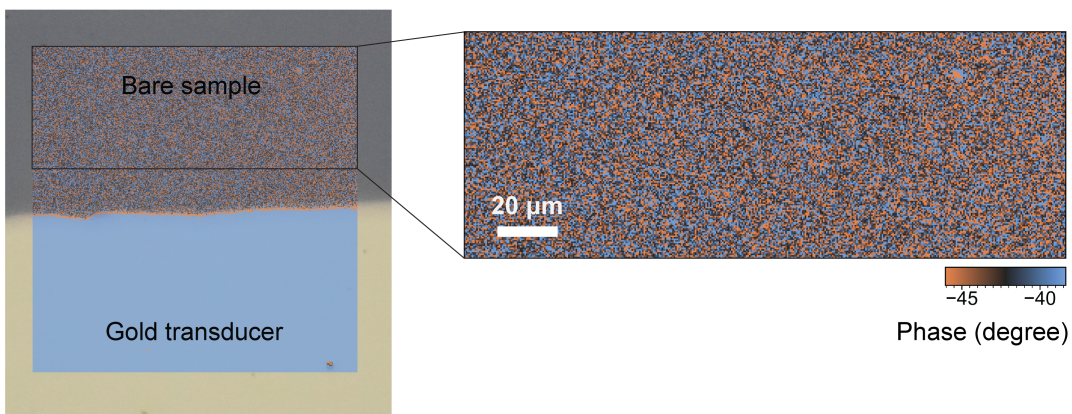


Figure S4: Map of the same NdNiO_3 film at room temperature. Some fluctuations due to noise are visible, but they visibly change on a smaller length scale than those observed at the transition. The strength of the fluctuations is a function of the objective aperture strength. This map was collected at $20\times$ magnification and the effective beam radius is around $1.5\ \mu\text{m}$.

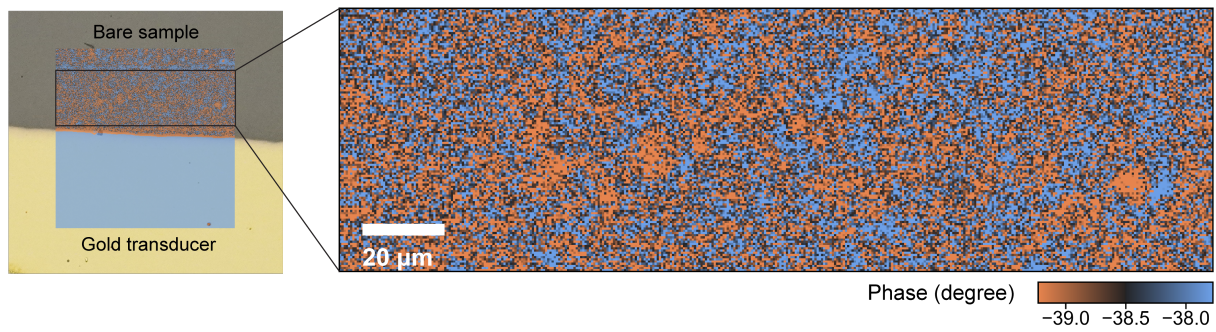


Figure S5: FDPR phase map at 113 K in the heating direction, showing the phase lag at a modulation frequency of 2 MHz, complementing the cooling-direction map in Fig. 4. The patterns show are distinctly different from those caused by noise at room temperature, indicating the presence of the phase transition.

Thermal Conductivity Data during Temperature Cycles

The data in Fig. 3b were collected over 3 cycles for cooling and 2 cycles for heating and averaged. The data without averaging is shown in Fig. S6.

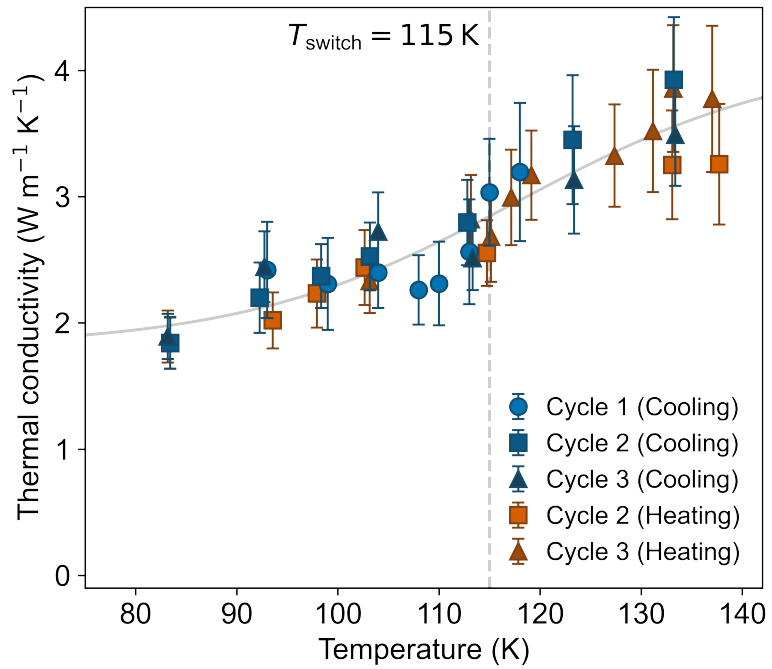


Figure S6: The thermal conductivity during heating and cooling cycles. The averaged values are presented in Fig. 3b.

Bootstrap Analysis for T_{switch}

We generate 10,000 synthetic datasets, sampling each data point from a normal distribution centered at its measured thermal conductivity value with a standard deviation given by its error bar. As shown in Fig. S7, the distribution of T_{switch} does not follow a perfect Gaussian function and exhibits slight asymmetry, potentially due to the slightly enlarged error bars at higher temperatures. We find the mean and standard deviation of T_{switch} is 115 K and 4 K.

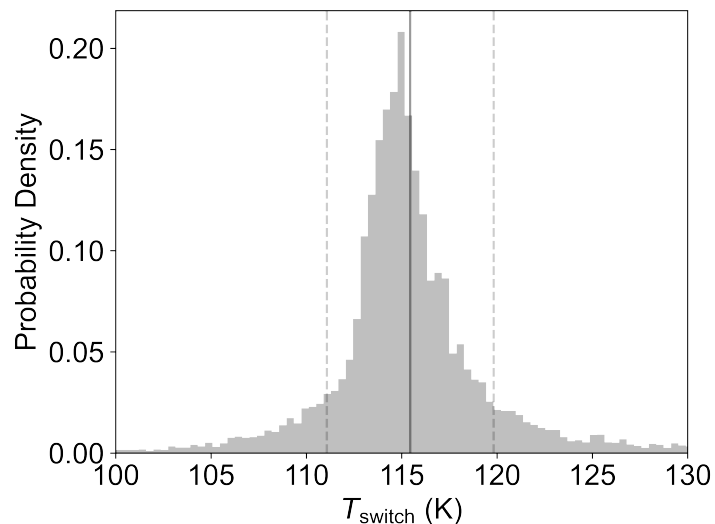


Figure S7: Histogram of bootstrap-derived T_{switch} values. Vertical lines mark the mean and $\pm 1\sigma$ interval. The switching temperature is determined to be $T_{\text{switch}} = 115 \pm 4$ K.

Uncertainty Analysis for Multivariate Fitting

In processing the FDTR data with Au transducer, the heat transfer model involves the thermal boundary conductance between the metal transducer and the thin film, G_{TF} , the thermal conductivity of the thin film, κ , and the thermal boundary conductance, G_{FS} . The correlations between these variables prevent us from fitting them together. Here, we present the uncertainty analysis^{S40} for fitting κ and G_{TF} and for fitting κ and G_{FS} by examining the confidence intervals in the multivariate fitting in Fig. S8. Because of the anti-correlations between κ and G_{TF} and between κ and G_{FS} , we fix the values of both thermal boundary conductances ($G_{\text{TF}} = G_{\text{FS}} = 45 \text{ MW m}^{-2} \text{ K}^{-1}$) and only fit the thermal conductivity.

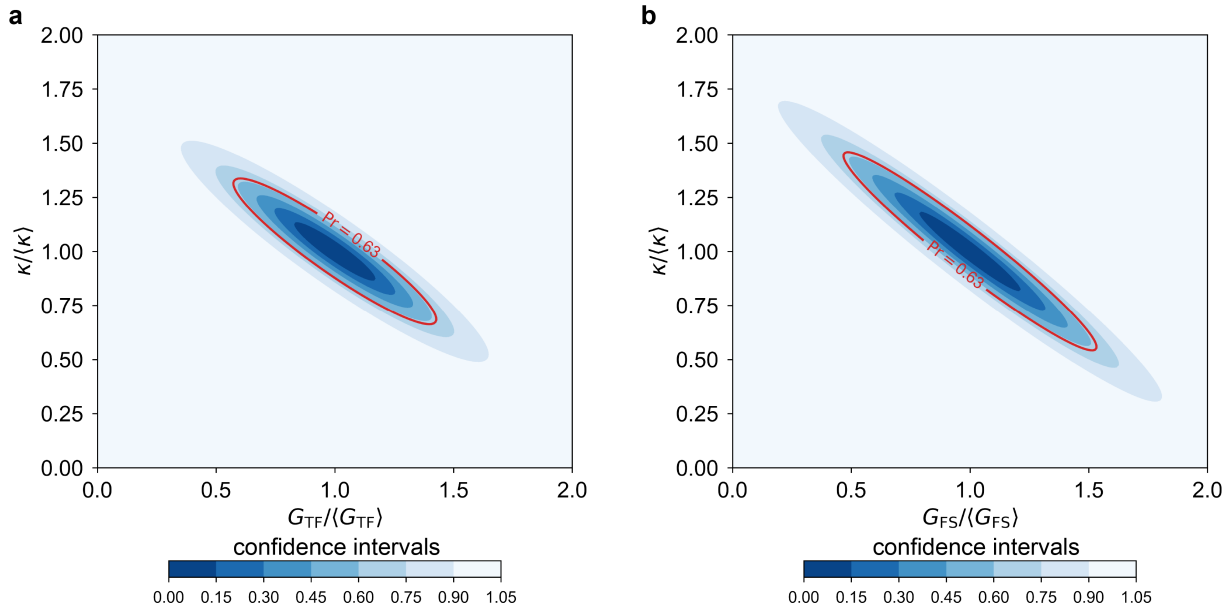


Figure S8: **a,b**, The confidence intervals for fitting κ and G_{TF} (**a**) and for fitting κ and G_{FS} (**b**) at 110 K. The contours correspond to the cumulative distribution function of a chi-squared continuous random variable evaluated at the same Mahalanobis distance. The Mahalanobis distance is defined by $D = (\mathbf{X} - \boldsymbol{\mu})^T \boldsymbol{\Sigma}^{-1} (\mathbf{X} - \boldsymbol{\mu})$, where \mathbf{X} is the random variable, $\boldsymbol{\mu}$ is the mean and $\boldsymbol{\Sigma}$ is the variance-covariance matrix. All non-fitting parameters are assumed to have a 3% uncertainty. The 0.63 confidence interval, equivalent to the generalized $1-\sigma$ confidence interval in the multivariate case, is marked in red. The bracket represents the mean value of the variable. We find that κ and G_{TF} and κ and G_{FS} are both anti-correlated, and that fitting the thermal conductivity of the thin film together with either thermal boundary conductance substantially increase the uncertainty in κ .

In processing the FDPR phase data, we choose D_a and G_{FS} as the fitting variables. This is because the sensitivity curves for D_a and G_{FS} possess distinctive frequency dependence (i.e. they are not simple rescalings of one another) in Fig. 2. We also calculate the variance-covariance matrix and present the corresponding confidence intervals for fitting D_a and G_{FS} in Fig. S9. The confidence intervals reveal essentially zero correlation, further supporting our fitting strategy for the FDPR data analysis.

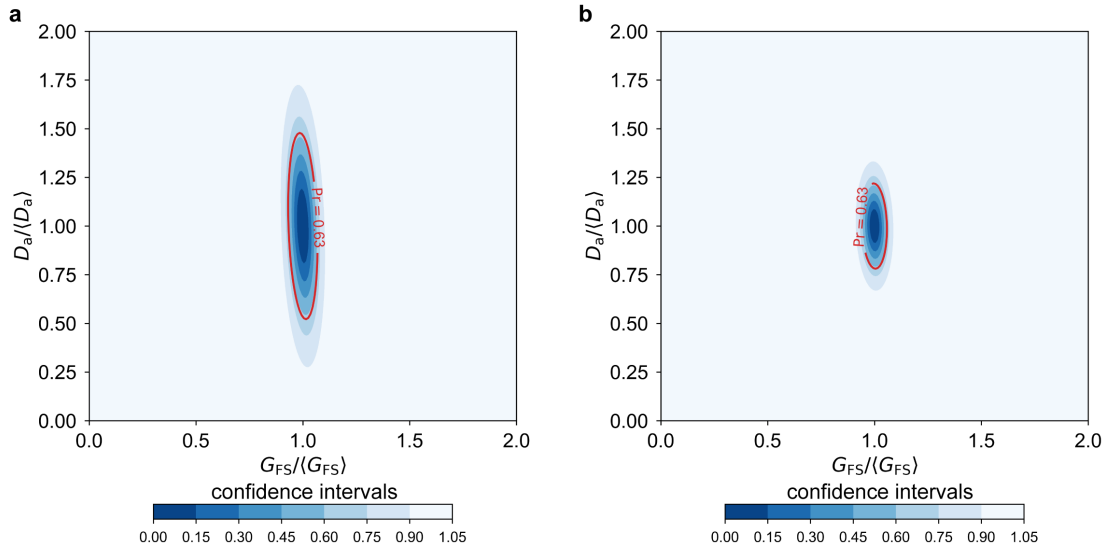


Figure S9: **a,b,** The confidence intervals for extracting G_{FS} and D_a from FDPR data at 108 K (**a**) and 133 K (**b**). Both contour plots reveal minimal correlation between G_{FS} and D_a .

Effect of Thickness on the Microscopic Domain Effect

We measure a 20.6-nm NdNiO_3 thin film on LaAlO_3 substrate grown via molecular-beam epitaxy. Four-probe resistivity measurements (Fig. S10d) show $T_{\text{MIT}} = 106 \text{ K}$ on cooling and $T_{\text{MIT}} = 145 \text{ K}$ on warming; both temperatures are slightly higher than in the original sample, and the hysteresis of 39 K is comparable to the original sample. We deposit a transducer layer of 77.8 nm Au and a 1.8 nm Ti adhesion layer via electron-beam evaporation (Denton e-beam evaporator). This procedure is consistent with that used for our original sample, expect that we used a Cr adhesion layer only on the LaAlO_3 substrate sample. We confirm the thickness of the film and the transducer layer, as well as the film's composition, using X-ray reflectivity (Fig. S10b,c) and X-ray diffraction (Fig. S10a) using a PANalytical Empyrean X-Ray Diffractometer. We measure the thermal conductivity across the MIT during heating and cooling to identify any hysteresis. We measure this sample using an incident pump power of 5.72 mW. The temperature rise for this pump power is expected to be very low.

Fig. S10 shows phase lag data and best fits for metallic and insulating states. The sensitivity analysis (Fig. S10f) shows that FDTR is much less sensitive to this sample's out-of-plane thermal conductivity, κ_{\perp} , than to that of our original sample because this sample is much thinner than the original sample, which correspondingly lowers its thermal resistance. Still, we observe no hysteresis in the out-of-plane thermal conductivity measurements (Fig. S10g). This result matches our thicker film, again suggesting a lack of percolation in the out-of-plane direction. We can therefore conclude that the anisotropy in the hysteresis is common to NdNiO_3 films of similar thicknesses to our original sample.

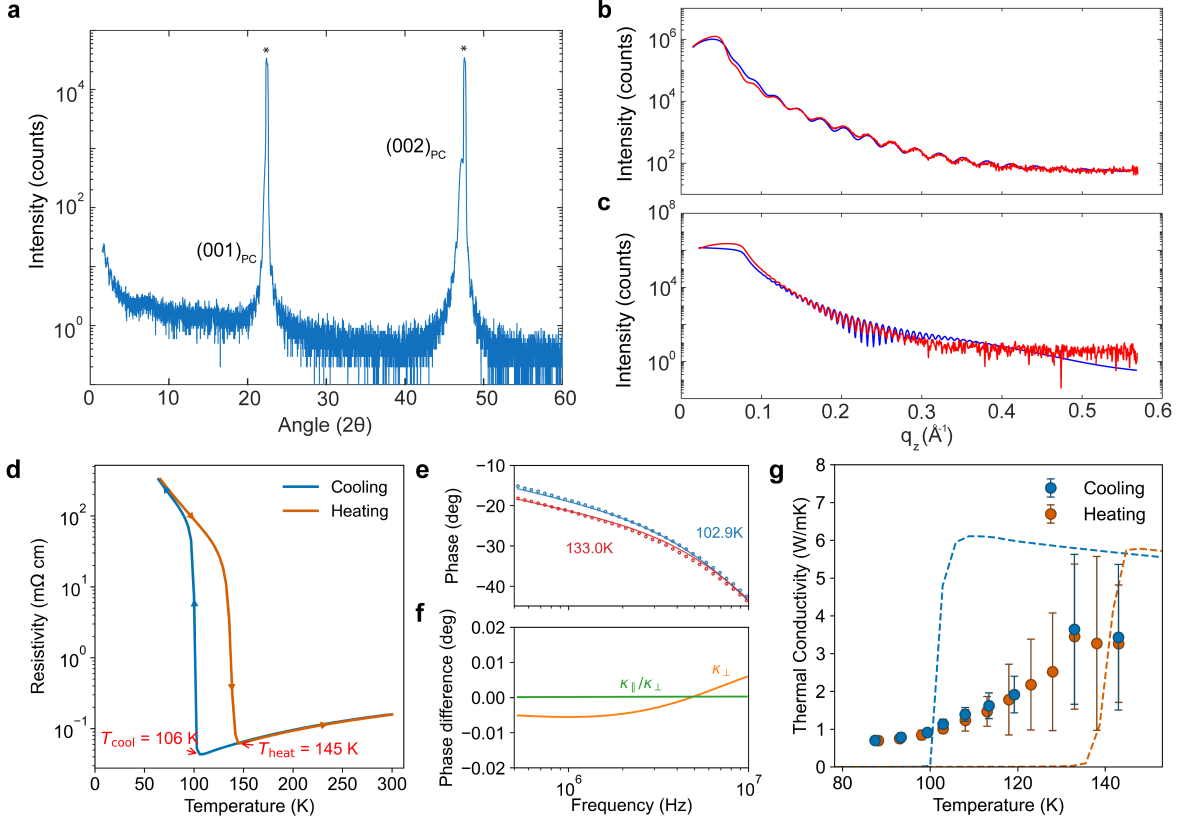


Figure S10: Characterization of thermal transport in a 20.6-nm NdNiO₃ thin film on LaAlO₃ substrate. **a**, X-ray diffraction pattern of the sample showing the pseudocubic (001) and (002) peaks. LaAlO₃ (001)_{PC} and (002)_{PC} peaks are marked with an asterisk (*). **b**, X-ray reflectivity data on the sample (red), with the best fit for a 20.6 nm thickness overlaid (blue). **c**, X-ray reflectivity data (blue) for the transducer layer with the best fit (red) overlaid, corresponding to 77.8 nm of Au and 1.8 nm of Ti. **d**, Temperature-dependent electrical resistivity showing $T_{MIT} = 106$ K on cooling and 145 K on heating, yielding a hysteresis width of 39 K. **e**, Example phase lag data and best fits from the metallic (red) and insulating (blue) phases. **f**, Sensitivity analysis for phase lag best fits at 133 K. Following the procedure in the main text, we increase the thermal conductivity by 1% and record the change in the modeled phase lag as a function of frequency. As with the 57.5-nm sample, the sensitivity to the in-plane thermal conductivity is nearly zero, and we see that the sensitivity to the out-of-plane thermal conductivity is smaller than that of the original sample. We attribute the decreased sensitivity to the reduced thickness of the new sample, which correspondingly lowers its thermal resistance. **g**, Out-of-plane thermal conductivity as a function of temperature, extracted from best-fit phase lag curves. Wiedemann-Franz law predictions for the electron contribution to in-plane thermal conductivity are overlaid (dashed lines). We again identify little hysteresis in the out-of-plane thermal conductivity between the cooling and heating measurements, a behavior consistent with the original sample.

Refractive Index of NdNiO₃

According to Ref.,^{S41} the real part of the dielectric constant of bulk NdNiO₃ is approaching a constant value of $\varepsilon_r = 1.7$ as the photon energy ω approaches 1 eV. This value remains nearly unchanged across temperatures both below and above the metal–insulator transition temperature. A similar asymptotic behavior has been observed in NdNiO₃/NdGaO₃ (110).^{S42} Therefore, we approximate the real part of the dielectric constant of the NdNiO₃ thin film with $\varepsilon_r = 1.7$ at photon energies of $\omega = 2.71$ eV (pump wavelength $\lambda = 458$ nm) and $\omega = 2.33$ eV (probe wavelength $\lambda = 532$ nm). As for the imaginary part of the dielectric constant, the optical conductivity measurements on a NdNiO₃ film on a LaAlO₃ (001) substrate in Ref.^{S43} indicates that $\varepsilon_i = 2.86$ at $\omega = 2.71$ eV and $\varepsilon_i = 3.15$ at $\omega = 2.33$ eV at 298 K. Notably, the imaginary dielectric constant between 2 eV and 3 eV varies minimally across temperatures below and above the metal–insulator transition. Hence, we obtain that $\varepsilon_i = 2.86$ at the pump photon energy and $\varepsilon_i = 3.15$ at the probe photon energy. Accordingly, the real and imaginary parts of the refractive index are $n = 1.59$, $\kappa = 0.90$ at the pump wavelength, and $n = 1.59$, $\kappa = 0.97$ at the probe wavelength. Consequently, the optical penetration depths for the pump and probe beams are 40 nm and 43 nm, respectively.

Frequency-Domain Photo-Reflectance for the Thin-Film-on-Substrate Geometry

The frequency-domain photo-reflectance signal is contributed by the carrier density part, the electronic temperature part, and the lattice temperature part,

$$\frac{\Delta R}{R} = \text{Re}\{A\bar{\rho} + B\bar{T}_{\text{el}} + C\bar{T}_{\text{ph}}\} \quad (\text{S1})$$

where $\bar{}$ denotes the weighted average by the probe beam profile, and A , B , and C are material-dependent real constants. As pointed out by Ref., [S23](#) in the modulation frequency range we choose (< 10 MHz), the electron-phonon coupling is strong enough such that $T_{\text{el}} \approx T_{\text{ph}}$. As a result, we only need to consider the contributions from the carrier and the lattice temperature,

$$\frac{\Delta R}{R} \approx \text{Re}\{\text{CCR } \bar{\rho} + \text{CTR } \bar{T}\} \quad (\text{S2})$$

where CCR is the coefficient of carrier-induced reflectance, and CTR = $B + C$ is the effective coefficient of thermoreflectance. In the following, we outline how to model the signal due to carriers and temperature.

We start with the dynamics of photo-excited carriers in a thin film described by,

$$\frac{d\rho}{dt} = D_{\text{a},z} \frac{\partial^2 \rho}{\partial z^2} + D_{\text{a},\parallel} \left(\frac{\partial^2}{\partial x^2} + \frac{\partial^2}{\partial y^2} \right) \rho - \frac{\rho}{\tau} + P \quad (\text{S3})$$

where ρ is the excited electron density, P is the number density of pump photons absorbed by the thin film per unit time, $D_{\text{a},\parallel}$ and $D_{\text{a},z}$ are the in-plane and out-of-plane ambipolar diffusivity, respectively, and τ is the carrier recombination time. Taking the Fourier transform of Eq. [S3](#) in the x- and y-directions, we obtain,

$$\frac{\partial^2}{\partial z^2} \tilde{\rho} - \Lambda \tilde{\rho} + \frac{\tilde{P}}{D_{\text{a},z}} = 0 \quad (\text{S4})$$

where $\tilde{P} = \frac{P_0\alpha}{h\nu_{\text{pump}}} e^{-\frac{\sigma_x^2 q_x^2}{8}} e^{-\frac{\sigma_y^2 q_y^2}{8}}$ and $\Lambda = \frac{D_{a,\parallel}}{D_{a,z}} q_\parallel^2 + \frac{1}{D_{a,z}\tau} + \frac{i\omega}{D_{a,z}}$. Here, P_0 is the absorbed pump laser power, $h\nu_{\text{pump}}$ is the photon energy, α is the inverse penetration depth of the pump laser beam, and σ_x and σ_y are the pump laser beam's radii along the x- and y-directions, respectively. The boundary condition at the two surfaces of the film is given by,

$$-D_{a,z} \frac{\partial \tilde{\rho}}{\partial z} + \tilde{\rho} S_j = 0 \quad (\text{S5})$$

where S_j ($j = 1, 2$) denotes the surface recombination velocities at the top and bottom surface, respectively. Note that the bottom surface corresponds to the interface between the thin film and the insulating substrate.

The solution to Eq. S4 takes the following form,

$$\tilde{\rho} = D e^{-\sqrt{\Lambda}z} + E e^{\sqrt{\Lambda}z} + F e^{-\alpha z} \quad (\text{S6})$$

where $F = \frac{P_0\alpha}{h\nu_{\text{pump}} D_{a,z}(\Lambda - \alpha^2)} e^{-(\sigma_x q_x^2 + \sigma_y q_y^2)/8}$ and,

$$D = \frac{-(D_{a,z}\alpha + S_1)(-D_{a,z}\sqrt{\Lambda} + S_2) + (-D_{a,z}\sqrt{\Lambda} + S_1)(D_{a,z}\alpha + S_2)e^{-(\sqrt{\Lambda}+\alpha)L}}{(D_{a,z}\sqrt{\Lambda} + S_1)(-D_{a,z}\sqrt{\Lambda} + S_2) - (-D_{a,z}\sqrt{\Lambda} + S_1)(D_{a,z}\sqrt{\Lambda} + S_2)e^{-2\sqrt{\Lambda}L}} F \quad (\text{S7})$$

$$E = \frac{-(D_{a,z}\alpha + S_1)(D_{a,z}\sqrt{\Lambda} + S_2) + (D_{a,z}\sqrt{\Lambda} + S_1)(D_{a,z}\alpha + S_2)e^{(\sqrt{\Lambda}-\alpha)L}}{(-D_{a,z}\sqrt{\Lambda} + S_1)(D_{a,z}\sqrt{\Lambda} + S_2) - (D_{a,z}\sqrt{\Lambda} + S_1)(-D_{a,z}\sqrt{\Lambda} + S_2)e^{2\sqrt{\Lambda}L}} F \quad (\text{S8})$$

with L denoting the thickness of the thin film.

We then take the inverse Fourier transform to obtain $\rho(\mathbf{r})$ and the signal measured by the probe beam is given by,

$$I_e(\omega) = \text{CCR} \frac{2\gamma}{\pi\sigma'_x\sigma'_y} \int \int_0^\infty \rho(\mathbf{r}) e^{-2x^2/\sigma'_x^2} e^{-2y^2/\sigma'_y^2} e^{-\gamma z} dz d^2\mathbf{r}_\parallel \quad (\text{S9})$$

where γ is the inverse penetration depth of the probe beam, and σ'_x and σ'_y are the probe beam radii along x- and y-directions, respectively. Note that we extend the upper limit of

the integration in the z-direction to infinity, as the light entering the substrate can be ignored given the fact that both penetration depths of the pump and probe beams are smaller than the film thickness. In oxide thin films, such as VO₂,^{S44} the electron mean free path is on the order of the lattice constant, and thus much shorter than the film thickness. Hence, we can assume isotropic diffusivity, such that $D_{a,\parallel} = D_{a,z} = D_a$, and $\Lambda = q_{\parallel}^2 + \frac{1}{D_a\tau} + \frac{i\omega}{D_a}$. Further assuming small surface recombination velocities (weak band bending), we have the following expression of the signal,

$$I_e(\omega) = \frac{\text{CCR}}{(2\pi)^2} \int \frac{P_0\alpha\gamma}{h\nu D_a(\Lambda - \alpha^2)} \left(\frac{1}{\alpha + \gamma} + \frac{D}{\sqrt{\Lambda} + \gamma} + \frac{E}{-\sqrt{\Lambda} + \gamma} \right) e^{-\frac{R_x^2 q_x^2}{4}} e^{-\frac{R_y^2 q_y^2}{4}} d^2 \mathbf{q}_{\parallel} \quad (\text{S10})$$

where

$$D = \frac{\alpha}{\sqrt{\Lambda}} \frac{1 - e^{-(\sqrt{\Lambda} + \alpha)L}}{-1 + e^{-2\sqrt{\Lambda}L}} \quad (\text{S11})$$

$$E = \frac{\alpha}{\sqrt{\Lambda}} \frac{-1 + e^{(\sqrt{\Lambda} - \alpha)L}}{-1 + e^{2\sqrt{\Lambda}L}} \quad (\text{S12})$$

and $R_x = \sqrt{\sigma_x^2 + \sigma'_x{}^2}$ and $R_y = \sqrt{\sigma_y^2 + \sigma'_y{}^2}$ are the effective beam radii along x- and y-directions, respectively. Eq. S10 is the formal expression of the carrier part of the signal. In Fig. S11, we present the representative spatial profiles of the carrier density. The probe-intensity-weighted integral of this distribution corresponds to the carrier part of the measured signal.

Next, we consider the temperature part of the signal $I_{\text{th}}(\omega)$. As derived in Ref.,^{S39} the phonon temperature profile within the thin film is expressed by,

$$\tilde{T} = \left(C e^{\sqrt{\lambda}z} + D e^{-\sqrt{\lambda}z} + F e^{-\alpha z} \right) e^{-\frac{\sigma_x^2 q_x^2}{8}} e^{-\frac{\sigma_y^2 q_y^2}{8}} \quad (\text{S13})$$

where $\lambda = i \frac{C_p \omega}{\kappa_{\perp}} + \frac{\kappa_{\parallel}}{\kappa_{\perp}} q_{\parallel}^2$, $F = \frac{1}{\kappa_{\perp}} \frac{P_0 \alpha}{\lambda - \alpha^2}$, and C_p is the volumetric heat capacity. Here, C and D are given by,

$$C = \frac{1}{2} \left[\frac{\alpha}{\sqrt{\lambda}} - \left(1 + \frac{M_4}{M_3} \right) \right] F \quad (\text{S14})$$

$$D = \frac{1}{2} \left[-\frac{\alpha}{\sqrt{\lambda}} - \left(1 + \frac{M_4}{M_3} \right) \right] F \quad (\text{S15})$$

Specifically, M_3 and M_4 are elements of the transfer matrix relating the temperature and heat flux at the bottom of the substrate to the temperature and the laser-heating-related term at the surface,

$$\begin{pmatrix} \tilde{T}_n(L_n) \\ \tilde{q}_n(L_n) \end{pmatrix} = \begin{pmatrix} M_1 & M_2 \\ M_3 & M_4 \end{pmatrix} \begin{pmatrix} \tilde{T}_1(0) \\ Fe^{-\frac{R_x^2 q_x^2}{4}} e^{-\frac{R_y^2 q_y^2}{4}} \end{pmatrix} \quad (\text{S16})$$

The construction of such a transfer matrix requires the heat capacity C_p , thickness L , and thermal conductivity components κ_{\parallel} and κ_{\perp} of each layer, as well as the thermal boundary conductance G between adjacent layers.

Consequently, the temperature part of the signal is written as,

$$\begin{aligned} I_{\text{th}}(\omega) &= \frac{\text{CTR} \gamma}{(2\pi)^2} \int \left(\frac{C}{\gamma - \sqrt{\lambda}} + \frac{D}{\sqrt{\lambda} + \gamma} + \frac{F}{\alpha + \gamma} \right) e^{-\frac{R_x^2 q_x^2}{4}} e^{-\frac{R_y^2 q_y^2}{4}} d^2 \mathbf{q}_{\parallel} \\ &= \frac{\text{CTR}}{(2\pi)^2} \int \left\{ \frac{1}{\lambda - \gamma^2} \left[\left(1 + \frac{M_4}{M_3} \right) \gamma - \alpha \right] + \frac{1}{\alpha + \gamma} \right\} \frac{P_0 \alpha \gamma}{\kappa_{\perp} (\lambda - \alpha^2)} e^{-\frac{R_x^2 q_x^2}{4}} e^{-\frac{R_y^2 q_y^2}{4}} d^2 \mathbf{q}_{\parallel} \end{aligned} \quad (\text{S17})$$

Finally, by summing Eq. S10 and Eq. S17, we obtain the total signal measured at different modulation frequencies in the experiment,

$$I(\omega) = I_e(\omega) + I_{\text{th}}(\omega) \quad (\text{S18})$$

We refer to the combined expression in Eq. S18 as the carrier and temperature model. We emphasize that, to the best of our knowledge, such a parallel treatment of charge and thermal transport in a thin film under laser irradiation has not been previously reported.

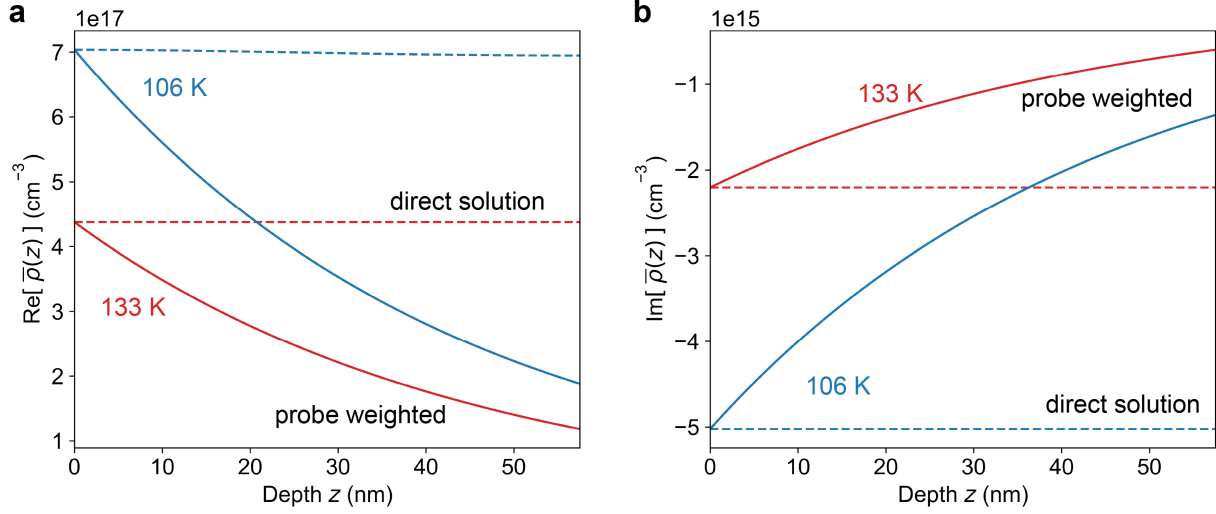


Figure S11: **a,b,** Real and imaginary parts of the photo-excited carrier density $\bar{\rho}(z)$ within the thin film at $f = 10.5$ MHz when the absorbed pump power $P_0 = 6$ mW. Solid lines represent the direct spatial profile $\bar{\rho}(z)$, while the dashed lines correspond to the carrier density weighted by the exponentially decaying probe intensity in the depth direction ($\propto e^{-\gamma z}$). The carrier part of the signal collected by the probe is given by $\text{CCR} \times \bar{\rho} = \text{CCR} \gamma \int \bar{\rho}(z) e^{-\gamma z} dz$. We rule out the possibility of a direct photo-induced metal-insulator transition due to the insufficient density of photo-excited carriers. Instead, the metal-insulator is temperature-driven.

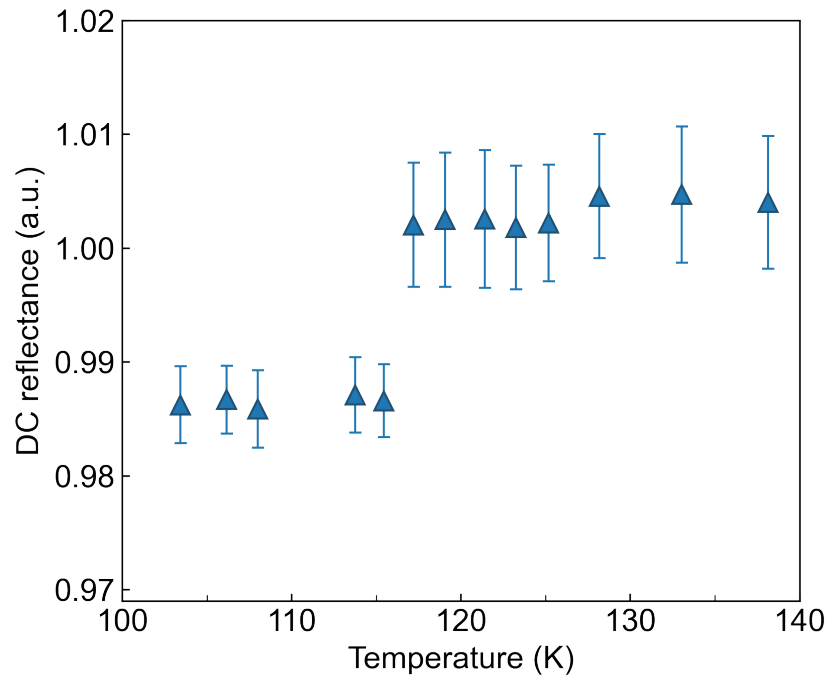


Figure S12: The DC photo-reflectance R as a function of temperature in FDPR measurements during heating. The error bars represent the standard deviations of the data across all modulation frequencies at the same temperature and indicate only a weak frequency dependence. A sudden jump in R is observed around 115 K, consistent with the transport measurements.

Fitting Analysis in FDPR

The total signal in Eq. S18 can be reorganized as,

$$I(\omega) = \text{CTR} \left(\bar{T} + \frac{\text{CCR}}{\text{CTR}} \times \bar{\rho} \right) \quad (\text{S19})$$

In fitting the phase data of the photo-reflectance to our model, the prefactor CTR does not influence the best, and the combined term $\frac{\text{CCR}}{\text{CTR}}$ effectively behaves as an independent variable. Therefore, we define,

$$A_\rho = \frac{\text{CCR}}{\text{CTR}} \quad (\text{S20})$$

By considering Eq. S2, we identify the physical meaning of A_ρ as the inverse of the temperature derivative of the carrier density,

$$A_\rho = \frac{\Delta T}{\Delta \rho} \approx \left(\frac{\partial \rho}{\partial T} \right)^{-1} \quad (\text{S21})$$

In practice, fitting both the amplitude and phase of the photoreflectance signals allows us to extract the specific values of CCR and CTR. We have demonstrated this capability in prior work^{S23} for bulk semiconductors. However, because of the strong anti-correlation between coefficient A_ρ and ambipolar diffusivity D_a in the nanoscale thin-film-on-substrate geometry, we cannot accurately determine A_ρ . Even so, this does not affect the relative change observed for D_a , irrelevant to the specific choice of A_ρ .

As a result, we need 3 unknowns to evaluate the carrier part of the signal: the ambipolar diffusion coefficient D_a , the inverse of the temperature derivative of the carrier density A_ρ , and the carrier recombination lifetime τ . The sensitivity to any variable x_i at the j th modulation frequency ω_j can be characterized by the phase difference,

$$\Delta\phi(\omega_j, x_i) = \arctan \left(\frac{\text{Im}\{I(\omega_j, x_i + \Delta x_i)\}}{\text{Re}\{I(\omega_j, x_i + \Delta x_i)\}} \right) - \arctan \left(\frac{\text{Im}\{I(\omega_j, x_i)\}}{\text{Re}\{I(\omega_j, x_i)\}} \right) \quad (\text{S22})$$

Here, we take the change in the variable, Δx_i , to be 1% of x_i , that is, $\Delta x_i = 0.01x_i$.

As illustrated in Fig. 2, the sensitivities to D_a and τ are similar in absolute magnitude but with opposite signs. This suggests that D_a and τ are anti-correlated in fitting. The sensitivities with respect to D_a and A_ρ exhibit a similar frequency dependence, differing only by a scaling factor on the order of unity. This indicates that D_a and A_ρ are positively correlated in fitting. As a consequence, we can fit only one out of the three variables with confidence. We argue that A_ρ and τ are more intimately connected to the band structure, which, within the energy range relevant to pump-excited electrons changes only minimally across the metal-insulator transition, whereas D_a is more strongly influenced by electron transport governed by electron-electron and electron-phonon interactions that are susceptible to metal-insulator transition. Hence, we treat A_ρ and τ as constants, and choose D_a as a fitting variable. Note that the thermal boundary conductance G_{FS} between the thin film and substrate and D_a are not correlated (see Fig. S9), and thus we include G_{FS} as an additional fitting parameter.

Sensitivity Analysis of LaAlO₃ Substrate

We find that our FDTR measurements are highly sensitive to the substrate parameters shown in Fig. 3a, measured on a substrate sample with no film. We show below the change in phase for a 1% increase in each of the shown parameters in the same way as calculated in Fig. 2d,e.

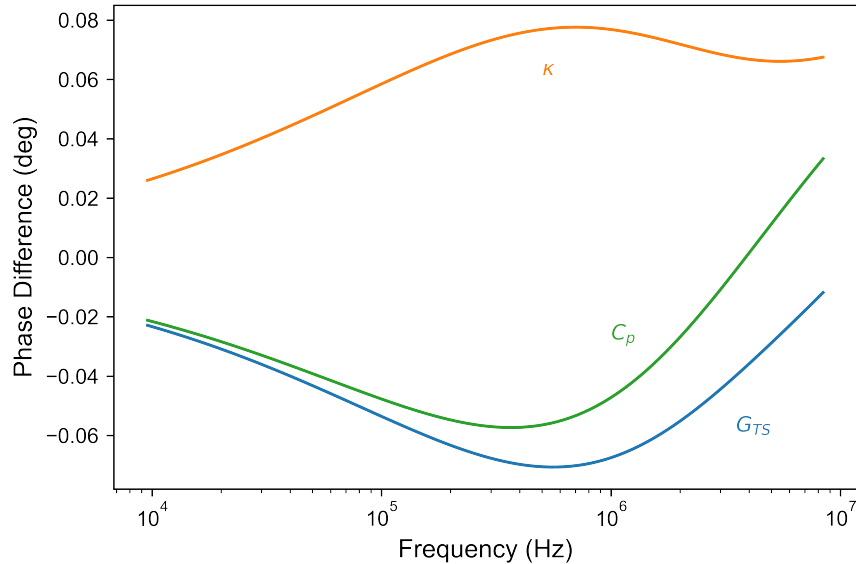


Figure S13: Sensitivity analysis of LaAlO₃ substrate parameters. These measurements were performed on a substrate without a film, coated in a transducer layer, and the results are shown in Fig. 3. Substrate thermal conductivity κ , volumetric heat capacity C_p , and the thermal boundary conductance between the transducer layer and the substrate G_{TS} are shown.

Negligible Electron–Phonon Coupling Effects in the Substrate Measurements

We quantify the effect of nonequilibrium electron-phonon coupling in the gold transducer layer on the phase lag using a two-temperature model^{S45,S46} to determine a modulation frequency regime where the Fourier-only model is sufficient. We observe that the effects of electron-phonon coupling are more pronounced as the modulation frequency becomes higher. The fits in Fig. 3a use a maximum frequency of 10^7 Hz. We reproduce those fits in Figs. S14b,c as well as fits on the same data using a cutoff frequency of 3.5×10^6 Hz, and we do not observe a significant difference between them. We therefore conclude that a Fourier-only model with $f < 10^7$ Hz is sufficient to exclude the influence of nonequilibrium electron-phonon coupling.

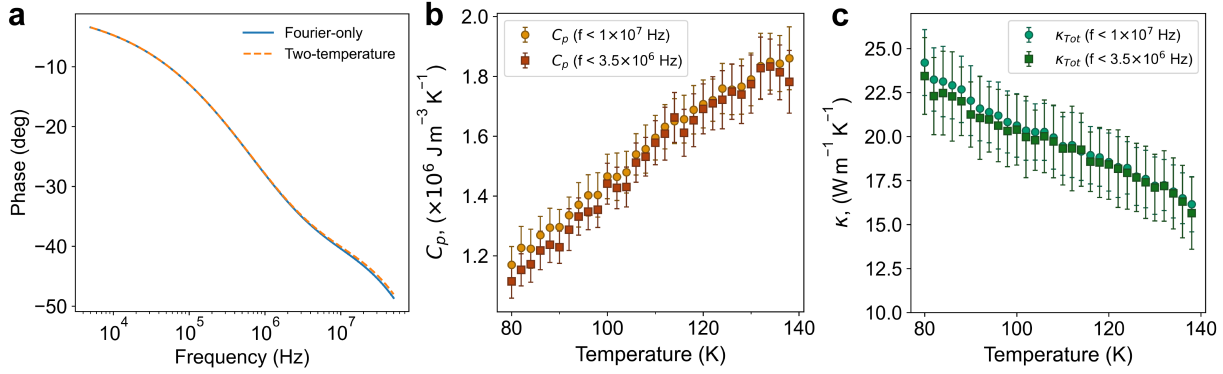


Figure S14: **a**, Modeled phase lag using the Fourier-only model (blue) and the two-temperature model including nonequilibrium electron-phonon coupling (orange) at 110 K. Parameters used: $\kappa_{\text{Au},e} = 112.8 \text{ W m}^{-1}\text{K}^{-1}$, $\kappa_{\text{Au},p} = 4 \text{ W m}^{-1}\text{K}^{-1}$, $C_{p,\text{Au}} = 2.16 \times 10^6 \text{ J m}^{-3}\text{K}^{-1}$, $g = 2 \times 10^{16} \text{ W m}^{-3}\text{K}^{-1}$, $\kappa_{\text{LaAlO}_3,e} = 0 \text{ W m}^{-1}\text{K}^{-1}$, $\kappa_{\text{LaAlO}_3,p} = 19.46 \text{ W m}^{-1}\text{K}^{-1}$, $C_{\text{LaAlO}_3,p} = 1.60 \times 10^6 \text{ J m}^{-3}\text{K}^{-1}$, $G_{pp} = 1.7 \times 10^8 \text{ W m}^{-2}\text{K}^{-1}$. **d**, Best fits for heat capacity, and **e**, thermal conductivity with using data with modulation frequencies $f < 1 \times 10^7$ Hz (the fits used in the main text), and with $f < 3.5 \times 10^6$ Hz. We find that the best fits obtained using data with $f < 1 \times 10^7$ Hz are similar to those using $f < 1 \times 10^7$, a cutoff that almost completely eliminates the influence of electron-phonon coupling.

Thermal Conductivity of the Gold Thin Film

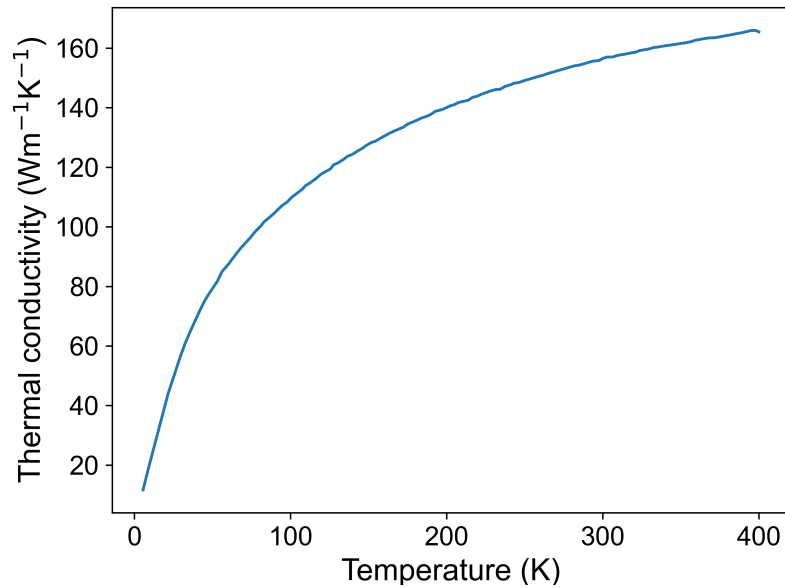


Figure S15: Thermal conductivity of 100 nm Au on glass using the Wiedemann-Franz law. The electrical conductivity of the gold transducer layer is measured with a four-point probe geometry using a Quantum Design Physical Property Measurement System.

Heat Capacity of NdNiO₃

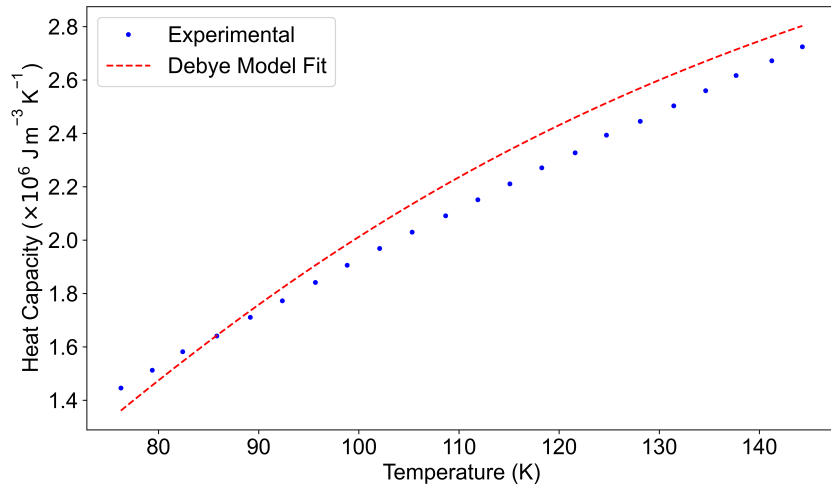


Figure S16: Heat capacity of NdNiO₃ as used to fit both the FDTR and FDPR data. Blue dots represent volumetric heat capacity taken from literature measurements on bulk NdNiO₃, obtained using semi-adiabatic calorimetry on a PPMS.^{S24} Although the phase transition occurs at a higher temperature in the bulk NdNiO₃ and the epitaxy strain in thin-film NdNiO₃ can alter the lattice dynamics, we believe that these factors only minimally affect the sensible component (i.e., the baseline) of the heat capacity. The red dashed line represents the Debye heat capacity prediction used to fix the heat capacity parameter in FDTR and FDPR measurements.

Data for Fig. 3b: Thermal Conductivity vs Temperature

The following tables provide the measured thermal conductivity κ as a function of temperature T , along with the associated uncertainty $\Delta\kappa$, for both cooling and warming cycles as shown in Fig. 3b. The data were averaged over three cooling cycles and two warming cycles (see Fig. S6).

Table 1: Thermal conductivity during cooling and warming

(a) Cooling			(b) Warming		
T (K)	κ ($\text{W m}^{-1}\text{K}^{-1}$)	$\Delta\kappa$	T (K)	κ ($\text{W m}^{-1}\text{K}^{-1}$)	$\Delta\kappa$
83.30	1.87	0.135	83.30	1.87	0.146
92.67	2.35	0.183	93.55	2.02	0.222
98.68	2.34	0.222	97.93	2.23	0.270
103.72	2.55	0.166	102.91	2.39	0.195
108.00	2.26	0.275	113.15	2.82	0.351
110.00	2.31	0.332	114.95	2.62	0.221
113.05	2.62	0.197	117.15	2.99	0.379
115.00	3.04	0.423	119.10	3.17	0.354
118.00	3.20	0.548	127.38	3.33	0.405
123.30	3.29	0.332	131.17	3.52	0.485
133.32	3.71	0.320	133.14	3.55	0.331
			137.39	3.52	0.375

TOC Graphic

